理學博士 學位論文

# Fabrication of Graphene by Using Thermal Plasma Jet: Flakes & Quantum Dots

## 열 플라즈마 젯을 이용한 그래핀 제조

2014 年 8 月

서울대학교 대학원

화학부 물리화학 전공

김 주 한

# Fabrication of Graphene by Using Thermal Plasma Jet: Flakes & Quantum Dots

## 열 플라즈마 젯을 이용한 그래핀 제조

지도교수 : 서 정 쌍

이 論文을 理學博士 學位論文으로 提出함

2014 年 8 月

서울大學校 大學院

化學部 物理化學 專攻

김 주 한

김주한의 理學博士 學位論文을 認准함

2014 年 8 月

| | | |
|---|---|---|
| 위 원 장 | 김 관 | (인) |
| 부위원장 | 서 정 쌍 | (인) |
| 위 원 | 홍 병 희 | (인) |
| 위 원 | 정 연 준 | (인) |
| 위 원 | 강 위 경 | (인) |

ABSTRACT

# Fabrication of Graphene by Using Thermal Plasma Jet: Flakes & Quantum Dots

Juhan, Kim
School of Chemistry
(Major : Physical Chemistry)
The Graduate School
Seoul National University

Graphene, which is a perfect two-dimensional material, has generated a great deal of interest due to its extraordinary properties and potential applications. Graphene shows novel electronic properties such as the room temperature quantum Hall effect and electrons that behave like massless Dirac fermions. Due to its high charge mobility and crystal quality combined with chemical and mechanical stability, graphene exhibits great promise for potential applications such as electric batteries, transistors, transparent electrodes, gas sensors, and solar cells. For further studies of the basic properties and future applications of graphene, we need a controllable and mass producible method of high quality graphene. Graphene has been prepared by various methods, such as micromechanical cleavage of bulk graphite, chemical vapor deposition on metal substrates, thermal decomposition of silicon carbide, gas phase synthesis using microwave plasma, plasma enhanced chemical vapor deposition, chemical exfoliation, and the solvothermal method. Among these methods, the last two methods are known as promising means for mass

production. However, both methods involve chemical processing. It is known that the crystallinity of graphene could be degraded by chemical processing. In gas phase synthesis, like using microwave plasma, no chemical process is involved except the thermal decomposition of the carbon source. It is a continuous process and, in principle, mass production is possible. However, the yield was very low, at 1.2%. The relatively low yield is probably due to the fact that the formation reaction could take place when the atomized carbon atoms collide randomly in the gas phase as they pass through a short reaction zone. We have developed a method to fabricate graphene flakes composed of high quality multi-layer graphene sheets using a thermal plasma jet system. A carbon atomic beam was generated by injecting ethanol into Ar plasma continuously; the beam then flowed through a carbon tube attached to the anode. Graphene was made by epitaxial growth where a carbon atomic beam, having the proper energy, collided with a graphite plate. The graphene fabricated was very pure and showed a relatively good crystalline structure. We have demonstrated that the number of layers of graphene sheets could be controlled by controlling the rate of ethanol injection. And as another carbon source, a relatively large amount of ethylene gas (500 sccm) was injected continuously into Ar plasma. Graphene containing about 3 atomic layers was produced and its average size was about 100 nm. The production rate of graphene based on the collected amount was about 1.5 g/h. Graphene was dispersed well in organic solvents such as ethanol, isopropyl alcohol and dimethylformamide (DMF) by sonication. We could make its thin films by electrophoresis, spray method and floating method in its dispersed solution. We also report a size-controllable and low-cost fabrication method of

graphene quantum dots (GQDs) using thermal plasma jet. A carbon atomic beam was generated by injecting a large amount (2.5 L/min) of ethylene gas continuously into Ar plasma. The beam was then flowed through a carbon tube (5-20 cm in length) attached to the anode, and then dispersed into a chamber. Carbon materials including GQDs were made by a gas phase collision reaction. The production rate of carbon soot was 40 g/hour for a 2.5 L/min injection rate. Almost all of carbon soot was dispersed in ethanol by sonication, while isolated GQDs were dispersed in ethanol by stirring with a stirring rod. Extraction of GQDs from carbon soot by dispersing in ethanol with a stirring rod is a very simple and low-cost process. The weight percent of GQDs in carbon soot, based on the amount extracted in ethanol, was about 10%. This means that the production rate of GQDs was about 4g/h. The average size of GQDs, with a relatively narrow size distribution, was controlled by varying the length of the carbon tube attached. It was about 10, 14, and 19 nm when the length was 5, 10, and 20 cm, respectively. Our method is a size-controllable, low-cost and mass-producible process. The electric structure based on the photoluminescence data of our GQDs had a singlet ground state and was in good agreement with that of carbyne. Our GQDs will disperse in organic solvents such as toluene, but not in water. The dispersion properties also support that our GQDs have carbyne-like edges. We proposed that the PL peaks observed can be attributed to electronic transitions between energy levels of the GQDs having carbyne-like edges.

**Keywords**: Graphene flake, Graphene Quantum Dots (GQDs), Thermal Plasma Jet (TPJ) ,

***Student Number***: 2007-20301

## CONTENTS

## LIST OF FIGURE

**oxygen.**

**Figure 6.12. Raman spectrum of GQDs, whose average size was 19 nm, measured by excitation with 514.5 nm Ar ion laser line. The G peak near 1596 $cm^{-1}$ is stronger than the D peak near 1353 $cm^{-1}$. The G/D intensity ratio is about 1.6.**

# CHAPTER 1. INTRODUCTION

## 1.1. The Structure of Graphene

Graphene is an atomically thin sheet of $sp^2$-bonded carbon atoms tightly packed in a two-dimensional (2D) honeycomb lattice and is a basic building block for graphitic materials of all other dimensionalities (Figure 1.1).[1] Honeycomb crystal lattice contains two carbon atoms in the every unit cell. The carbon-carbon bond length in graphene is about 0.142 nm and graphene sheets stack to form graphite with an interplanar spacing of approximately 0.334 nm (Figure 1.2).[2] Graphene was discovered in 2004 by scientists at the University of Manchester in England[3] and has generated great interest throughout a various range of scientific disciplines because of its remarkable properties and numerous potential applications.

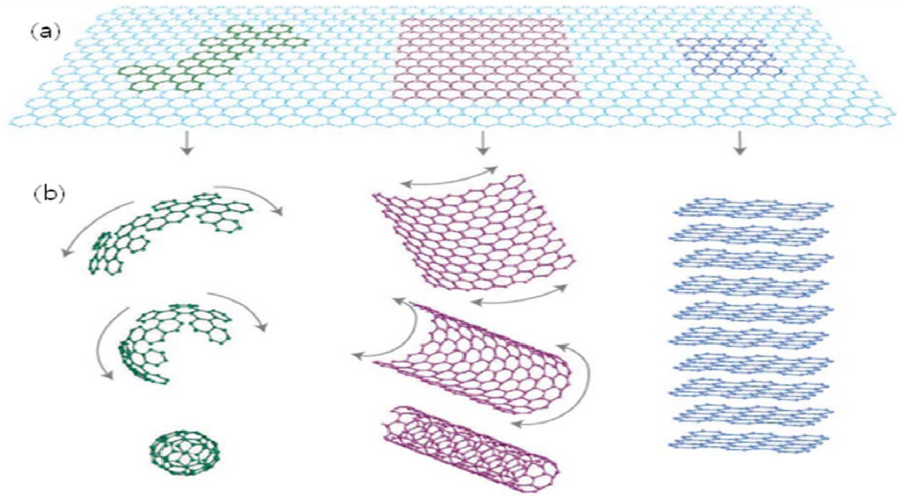


**Figure 1.1. (a) Graphene is a 2D building material for carbon materials of all other dimensionalities. It can be wrapped up into (b) 0D buckyballs, rolled into 1D nanotubes or stacked into 3D.** [1]

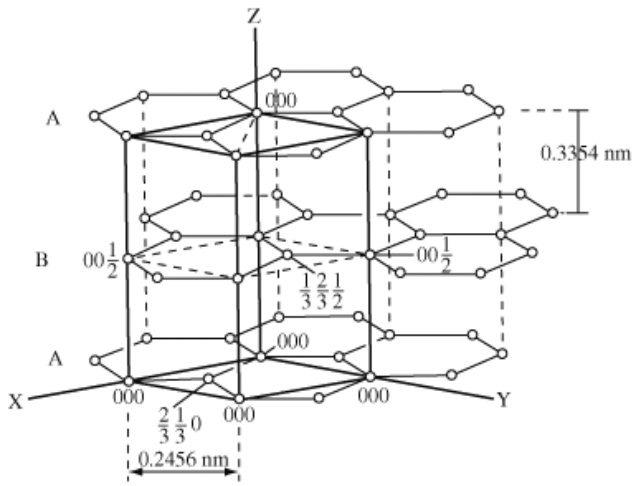


**Figure 1. 2. The structure of hexagonal (Bernal) graphite, showing the unit cell.** [2]

## 1.2. The Properties of Graphene

Graphene has a remarkably high electron mobility, with reported values in excess of 200,000 $cm^2 \cdot V^{-1} \cdot s^{-1}$ at a carrier density of $10^{12}$ $cm^{-2}$ and the mobility is nearly independent of temperature between 10 K and 100 K.[5-9] For comparison, electrons travel through Si and high-speed GaAs at 1500 and 8500 $cm^2 \cdot V^{-1} \cdot s^{-1}$ respectively.[10] Furthermore, charge carriers can be tuned continuously between electrons and holes in concentrations[1] up to $10^{13}$ $cm^{-2}$. The electrical resistivity of a graphene sheet is $10^{-6}$ Ω·cm, which is less than the resistivity of silver, the lowest resistivity material known at room temperature.[8] Graphene is a semi-metal and zero-gap semiconductor (Figure 1.3).[4]

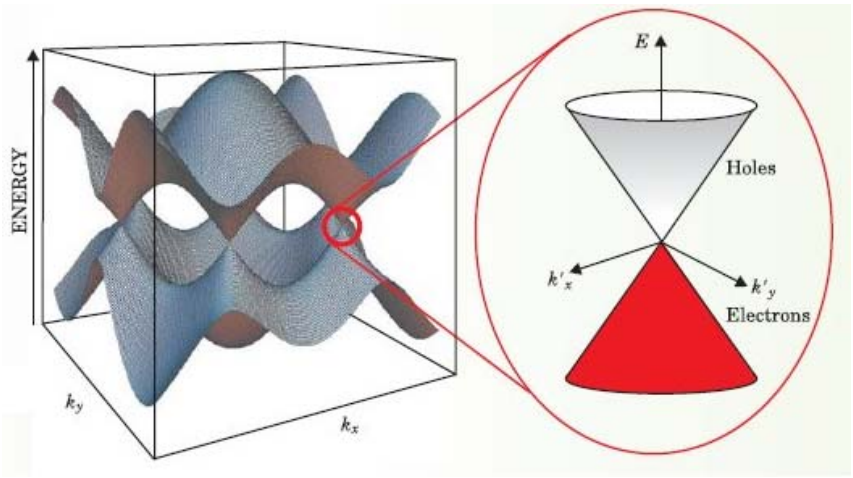


**Figure 1. 3 The 3D bandstructure of graphene.[4]**

Graphene also exhibits a Young's modulus (stiffness) of 1 TPa (150,000,000 psi)[10] and has a breaking strength over 100 times greater than a hypothetical steel film of the same (incredibly thin) thickness.

The thermal conductivity of graphene is one of the most important properties for applications in graphene research. The thermal conductivity[11] of single-layer graphene was usually measured between 5000 and 6000 $Wm^{-1}K^{-1}$. As density of electric charge in non-dopping graphene is relatively low, its effect of thermal conductivity excluded. Generally, thermal conductivity of graphene depends on phonon transport by two categories: Diffusive conduction at high temperature and ballistic conduction at low temperature.

The unique optical property of graphene is one of the biggest reasons to be motivated in graphene research since scientists observed graphene sheet from optical microscope on silicon substrate covered thin film Silicon oxide ($SiO_2$). An interference effect by multiple reflections of light in the silicon oxide film and graphene causes that single-layer graphene (absorbing $\pi\alpha \approx 2.3\%$ of white light, where $\alpha$ is the fine-structure constant) can be observed from general optical microscope.[12] The other surprising optical property is that the opacity of graphene film increases by exactly fine structure constant depending on graphene layer number.

Raman spectroscopy has been used to characterize the crystalline structure and number of layer of the graphene produced. In Raman spectra, graphene from graphite has the main peak of the G band peak at ~ 1584$cm^{-1}$ , G' band peak at ~ 2700$cm^{-1}$. The G band is the $E_2$ vibration mode, the G' band is 2nd-order two-phonon mode.

## 1.3. Synthesis Methods of Graphene

### 1.3.1. Scotch tape Method

In 2004, graphene was first exfoliated mechanically from graphite by the Manchester group.[3] They used adhesive tape to repeatedly split graphite crystals into increasingly thinner pieces. This simple technique has been widely credited for the explosive growth of interest in graphene and giving high structural and electronic quality graphene, which currently reach millimeter size even though tedious and time-consuming process. After the tape with attached transparent graphene flakes was dissolved in acetone, the flakes including monolayers were sedimented on a silicon wafer. graphene becomes visible under an optical microscope when deposited on a $SiO_2$ substrate with a specific oxide thickness of 300 nm. However, this method is very difficult to produce in large scales and quantities for wide range of application in industry.

### 1.3.2. Epitaxial growth Method

There are two main methods to synthesis graphene by epitaxial growth. The first method is “epitaxial growth on silicon carbide (SiC).” Epitaxial growth on silicon carbide (SiC) is a very favorable method for large-scale production of graphene. In this method, single crystal SiC substrates are heated to high temperatures (>1,100 °C) under low pressures (~$10^{-6}$ torr) to reduce it to graphene.[12-14] This epitaxial growth method has the advantage that the direct growth of graphene on an insulating substrate but the characteristics of graphene produced by this method are poor than mechanically exfoliated graphene because the various growth parameters of SiC substrates and epitaxial growth are highly dependent on the influence of the effect of interface on graphene.[15,16]

### 1.3.3. Chemical Vapor deposition method.

Another epitaxial growth method of producing graphene is chemical vapor deposition (CVD) method. This method uses carbon source and the atomic

structure of a metal substrate (Ni, Cu, Pt) to seed the growth of the graphene sheet. Hong's group produces few-layer graphene exceeding 1 $cm^2$ (0.2 sq in) in area by using chemical vapor deposition on thin nickel catalyst with methane as a carbon source.[17] After growing-graphene step, most of the nickel substrate is then etched away and graphene sheets are transferred to other substrates. The transferred graphene films show very low sheet resistance of 280Vper square, with 80 % optical transparency. An improvement of this technique has used copper foil where the growth automatically stops after a single-layer graphene at very low pressure.[18,19]

### 1.3.4. Chemical method

Graphene was first obtained from reduced Graphite oxide (GO) which was first produced by Ruoff research group from the Hummer's method[20] in 2006.

Even though this method had had a serious problem as aggregation phenomenon during reducing process by instability, Wallace[21] group suggested the result improved for the problem by controllable pH value.

A great advantage of the above mentioned method can produce single-layer

graphene at a low cost and control producing scale. In addition, it can obtain graphene by a more simplified process from graphite more than mechanical method, and produced graphene in this way can be used as a reinforcing agent[22] of composite material.

The Deposition is a method that can produce a various films from single film to overlapping films of high density using chemically modified suspension of graphene, Huang's group[23] of Northwestern University discovered depositing technique using the Langmuir Blodgett assembly of GO.

Dai's group[24] in Stamford University also performed a similar research that is one layer by layer assembly using Langmuir-Blodgett technique and substrate bias voltage. In Dai's lab, the exfoliated graphite was separated by the NaCl water. Exfoliated graphite by filtration was exposed to fuming sulfuric acid (oleum) at room temperature, and then washed acid. The sample was ultra-sonicated in dimethylformamide (DMF) of tetrabutylammonium hydroxide (TBA). The suspension was then centrifuged to take care of the product, which consists of multilayer graphite crystals in TBA solution. The single-layer graphene sheets were obtained in the supernatant. This step

nudges the piece of the graphene sheets by inserting (intercalating) oleum and TBA molecules among the atomic planes to obtain single-layer and multi-layer graphene.

On the other hand, Coleman group[25,26] has studied that graphite would be striped to pieces using a specific organic solvent such as N-methyl-pyrrolidone without any oleum and TBA agents. The obtained the graphene sheets of Coleman's lab in that research consist of fewer than five layers and 3 percent of flake obtained single-layer sheets from water-surfactant solutions was used to disperse and exfoliate graphite. The results could be a scalable method to obtain unoxidized single-layer graphene from graphite.

Yang's group[27] at the University of California in Los Angeles improved a method of placed graphite oxide paper in a solution of pure hydrazine (a chemical compound of nitrogen and hydrogen) which seperate the graphite oxide paper into single-layer graphene. Kaner's and Yang's lab use hydrazine as the solvent. The obtained graphene using the hydrazine solution is also a more efficient electrical conductor. The chemically modified graphene oxide was from Graphite powder based on a modified Hummers' method. In

summary, the dispersion solution of graphite oxide in water was heated with repeated ultrasonication, and filtered then under vacuum. After the dried black graphite oxide film was dispersed into hydrazine solution, the suspension was spin-coated onto substrates, and then thermally annealed to convert graphene. Yang reported the field-effect devices produced by conventional photolithography display currents that are three orders of magnitude higher than the officially reported using fabricated graphene chemically. It can be also a scalable and a far too easy method for the coverage of the graphene sheets to alter the concentration and composition of the hydrazine solution. Moreover, the hydrazine method preserves the integrity of the sheets, producing the large area graphene sheet, 20 ㎛ by 40 ㎛.

## 1.4. The Application of Graphene

### 1.4.1 Transparent conducting electrodes

It is expected that graphene may prove capable of replacing ITO (Indium Tin Oxide) glass as a transparent conducting electrodes because of graphene's good electrical conductivity and high optical transparency. The transparent graphene electrodes may be applied to the liquid crystal displays, organic photovoltaic cells, touchscreens and organic light-emitting diodes field. And graphene has excellent mechanical strength and flexibility, so application of a flexible display is possible.[28,29]

### 1.4.2 Transistors

Since graphene has unique energy band structure, graphene indicates a bipolar characteristic that the concentration of the electron and the hole can be adjusted continuously. Generally, a silicon substrate that used as the back gate of the FET (Field Effect Transistor) is the most studied, and graphene FET indicates a higher electrical mobility than silicon-based device. Also the first top-gated FET (on–off ratio of <2) was demonstrated in 2007.[30] In 2010, the

IBM researchers announced transistors with an on/off rate of 100 GHz.[31]

### 1.4.3 Gas Sensor

It is very important to detect gas-molecules in various fields such as environmental monitoring, energy industry and aerospace. Recently a carbon materials or semiconductor nanowire-based sensors are in the spotlight as the potential materials of the next generation for gas sensor. Sensors utilized nanomaterial feature very small in size, low power consumption and simple manufacturing. Especially graphene has excellent detection capability for the $NO_2$, $NH_3$, $H_2O$, CO and $H_2$. The gas-molecule absorption causes a change of electrical resistance in graphene sensors. Graphene has high electrical conductivity and low noise, which makes this change in resistance detectable.[32]

### 1.4.4 Solar cells

Graphene has unique properties of high electrical conductivity, non-toxic, low-cost and optical transparency. These properties make graphene a better

candidate material for solar-cell than other carbon materials. Because this graphene only absorbs 2.3% of visible light and graphene is a zero-bandgap semiconductor whose charge carriers are delocalized over large areas, it is a candidate for applications as a transparent conductor.[33]

### 1.4.5 Corrosion inhibitor

Currently, it was reported that graphene nanosheets can use a corrosion inhibitor to prevent corrosion of metal.[34] Copper coated single-layer graphene grown via chemical vapor deposition is seven times lower corrosion resistance than pure copper and in case of multilayer graphene, it is twenty times more excellent corrosion resistance, respectively. Such coating techniques can be applied to a variety of metals and do not depend greatly on the surface roughness of metal. And uniform large-area graphene synthesis and transfer through the process to get additional corrosion protection is expected to improve performance.

### 1.4.6 Energy storage device

In recent years, many studies are being made in the field of energy storage applications for graphene include super capacitors and batteries.[35-38] For graphene-based carbon materials may be made a super capacitor electrode of 0.34nm in thickness and from 100nm to 10μm in length. This materials have a large surface area(2600 ㎡/g). Also graphene can be functionalized by chemical reaction and can obtain an induced pseudo-capacitance by surface of the grafting or polymerization process similar to oxidation-reduction reaction. Graphene has drawn attention in current year for Li ion batteries due to high specific capacity, long cycle life, fast charge, high discharge capacity.

### 1.4.7 Other applications

Graphene can be envisioned for use in many different fields. The material can be used as additives in composite materials to increase strength and conductivity for plastic and metal. And aside from this, graphene can be utilized in hydrogen storage device, biological engineering, support membranes for Transmission Electron Microscopy, saturable absorber for ultrafast pulsed lasers and ultrafiltration membrane.

### 1.5 The Properties of Graphene Quantum Dots (GQDs)

Recent researches have led to the development of carbon dots (C-dots) that compose quasi-spherical nanoparticles with sizes smaller than 10 nm.[39-54] They have several favorable properties, such as quantum confinement effect, size and wavelength-dependent luminescence emission and a facile synthesis. In addition to these characteristics, graphene quantum dots (GQDs, graphene sheets smaller than 100 nm[55]), as a kind of C-dots, have excellent properties (high electron mobility, good thermal conductivity, excellent mechanical strength and chemical stability) of graphene sheets. GQDs suspensions typically show a broad UV-vis absorption with weak shoulders at 280 and 330 nm, similar to one previously reported.[56] The PL spectra are generally dependent on excitation wavelength, the PL peaks shifted to longer wavelengths with a maximum PL intensity as the excitation wavelength was increased.[57-60] The HOMO-LUMO energy gap of GQDs depends on the size of the graphene flakes. The energy gap decreases gradually as the size of GQDs increases, so different size GQDs have different emission spectra. Beside the size of GQDs, the pH of the GQDs suspensions also influences the

maximum PL intensity of GQDs. Pan *et al*. reported that, under alkaline conditions, the GQDs emitted strong PL whereas, under acidic conditions, the PL was nearly completely quenched.[58] In addition, reduction treatment,[60] thickness of graphene flakes[61] and Oxygen plasma etching can influence the PL intensity of GQDs. These properties of GQDs make them excellent materials for the construction of electron donors and electron acceptors in organic photovoltaic devices, catalyst for the oxygen reduction process, biosensors, bioimaging, and electronic devices.[62-71]

### 1.6 Synthetic Methods of GQDs

GQDs have been prepared mainly by top-down and bottom-up methods. Top-down methods refer to the cutting of graphene sheets into GQDs by hydrothermal, chemical reaction or plasma treatment. On the other hand, bottom-up approaches involve the synthesis of conjugated carbon atoms to compose GQDs (Figure 1.4).

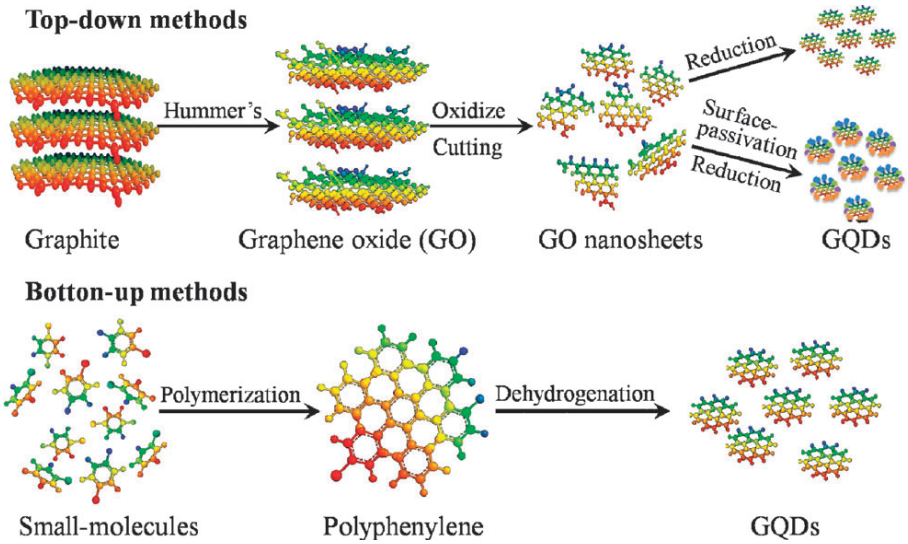


**Figure 1.4. Top-down and bottom-up methods of GQDs synthesis**[72]

### 1.6.1. Top-down methods of GQDs

In 2010, Pan *et al*. reported hydrothermal route for cutting graphene sheets into blue-luminescent GQDs.[58] The large graphene oxide sheets were cut into graphene flakes by chemical oxidation method using sulfuric acid and nitric acid. To obtain GQDs, oxidized small size graphene flakes were reduced by hydrothermal reaction. The size of GQDs was approximately 10 nm and consisting of 1-3 layers and has blue photoluminescence. Shen *et al*. developed surface-passivated GQDs using polyethylene glycol by hydrothermal reaction.[57] Zhu *et al*. prepared GQDs (approximately 5 nm, 1 or

2 layers) with green photoluminescence by solvothermal reaction[70]. GQDs were also produced by hydrazine hydrate reduction of oxidized small graphene sheets with their surface passivated by polyethylene glycol.[69]

Another unique approach to preparing GQDs is "oxygen plasma treatment method". Gokus group reported that strong PL intensity could be induced in single-layer graphene sheet using an oxygen plasma[61]. Graphene flakes isolated from graphite by mechanical exfoliation were exposed to oxygen plasma for 1~6 seconds. The PL mapping image obtained in confocal mode revealed that spatially uniform broadband PL feature for long exposed times (5~6 s). Chen *et al.* claimed that the fluorescence intensity was dependent on the ionic strength and pH, as a result, they synthesized graphene oxide nanosheets with visible and near-infrared fluorescene[73]. Cut of carbon fibers[69] or using self-assembled block copolymer[74] may also be categorized as a top-down method.

### 1.6.2. Bottom-up methods of GQDs

In 2010, Xin Yan *et al*. at the Indiana University, reported that, the synthesis of large colloidal graphene quantum dots with a uniform and tunable size through solution chemistry. They started from small-molecule precursors, such as 3-iodo-4-bromoaniline and other substituted benzene derivatives. GQDs consist of graphene moieties containing 168, 132, and 170 conjugated carbon atoms, respectively (Figure 1.5(a)). The stabilization of the resultant graphenes is achieved by multiple 2′,4′,6′-triakyl phenyl groups covalently attached to the edges of the graphene moieties.[75]

Another bottom-up approach was reported by Ruili Liu at the Max-Planck-Institute fur Polymerforschung[76]. They synthesized GQDs with a uniform size of ～60 nm diameter and 2~3 nm thickness by using unsubstituted hexa-*peri*-hexabenzocoronene (HBC) as the starting carbon materials by a process of carbonization, oxidization, surface functionalization and reduction (Figure 1.6).

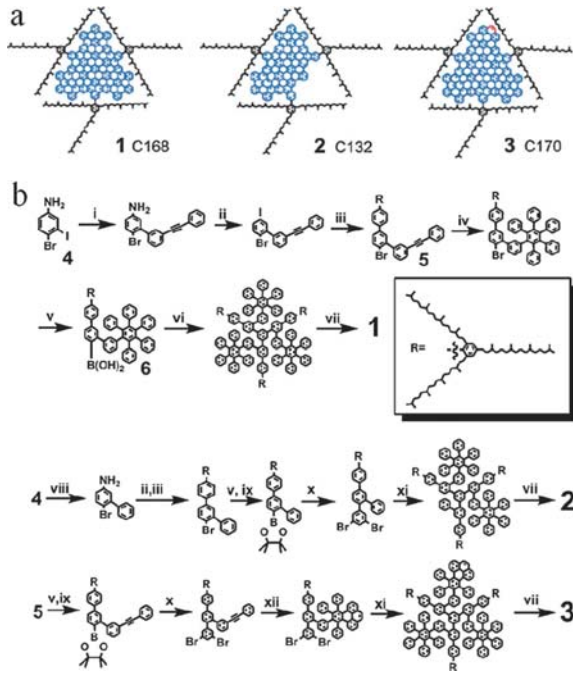


**Figure 1.5. (a) Uniform and tunable size of GQDs. (b) Synthesis step of GQDs 1-3 of (a)[75]**

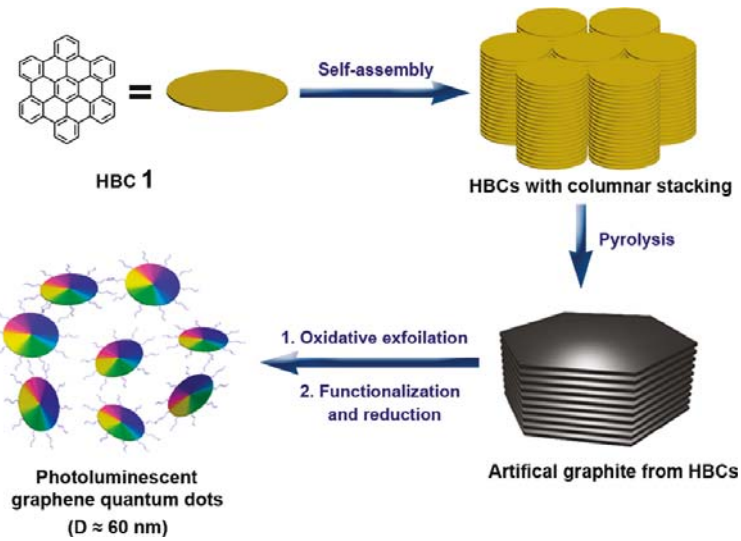


**Figure 1.6. Processing Diagram for the Preparation of Photoluminescent GQDs by Using HBC (1) as Carbon Source[76]**

# CHAPTER 2. EXPERIMENTAL

## 2.1. Fabrication of graphene flakes using a thermal plasma jet system

The thermal plasma jet is based on the atomization of gaseous mixture generated by arc discharge. Figure 2.1 shows a schematic of our thermal plasma jet system. A non-transferred thermal plasma system was operated by a direct current. Ar gas (99.999%) was used as a plasma gas and the flow rate of Ar gas, which was controlled by mass flow controller (DFC-4000, Flow Tech Co.) was 13.5 ksccm. Thermal plasma of Ar was generated by applying a high voltage of ~3 kV between a zirconium-containing tungsten cathode and a copper anode. The thermal plasma jet was stabilized by DC 180-210 A. The Ar plasma jet flowed into a Cu anode nozzle whose inner diameter was 6 mm, then continued through an attached carbon tube (5 mm in inner diameter and 50~300 mm in length). A well polished graphite plate was placed in the path of the plasma gas flow, perpendicular to the attached carbon tube. The distance between the end of the attached carbon tube and the graphite plate varied from 1 to 15 cm. Ethanol was used as a carbon source and inserted continuously in thermal plasma jet inlet. The flow rates of ethanol, which was

controlled by a syringe pump (Syringe Pump NE-1000), was 0.01~ 0.5 mL per min. Produced graphene flakes soot was harvested through a wall of thermal plasma chamber. Graphene flakes were analyzed by using a scanning electron microscope (SEM; JEOL ltd. JSM6700F (10 kV)), a high-resolution transmission electron microscope (JEOL, JEM-3000F (300 kV)), and Raman spectroscopy. Raman spectra were observed by using a micro-Raman system equipped with a homemade sample stage, a monochrometer (SPEX 500 M), and a CCD camera cooled with liquid nitrogen (Roger Scientific 7346-001 Model). Raman spectra were observed by excitation with a 514.5 nm laser line. The incident laser power on the sample was approximately 100 μW, and the acquisition time was 100 s.

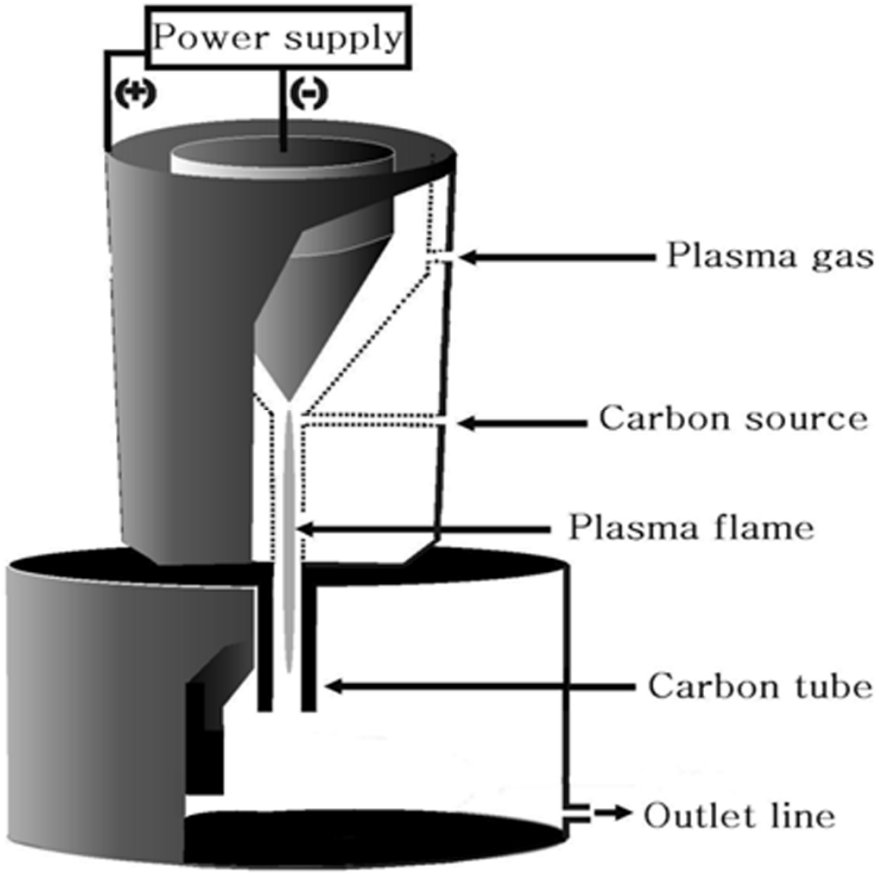


**Figure 2. 1. A schematic of the thermal plasma system for the continuous production of graphene flakes.**

## 2.2. Fabrication of dispersible graphene in organic solvents using thermal plasma jet system

The thermal plasma jet system used here is the same one as reported.[77] A non-transferred thermal plasma system was operated by a direct current. Ar gas (99.999%) was used as a plasma gas and the flow rate of Ar gas, which was controlled by mass flow controller (DFC-4000, Flow Tech Co.) was 13.5 ksccm. Thermal plasma of Ar was generated by applying a high voltage of ~3 kV between a zirconium-containing tungsten cathode and a copper anode. The thermal plasma jet was stabilized by DC 210-300 A. The Ar plasma jet flowed into a Cu anode nozzle whose inner diameter was 6 mm, then continued through an attached carbon tube (5 mm in inner diameter and 200 mm in length). A well polished graphite plate was placed in the path of the plasma gas flow, perpendicular to the attached carbon tube. The distance between the graphite plate and the end of the attached carbon tube was 10 cm. Ethylene gas was inserted continuously (500 sccm) as a carbon source into the torch using a mass flow controller. Produced graphene flakes soot was harvested through a wall of thermal plasma chamber. A 45 mg of as produced garphene

flakes was ultrasonically dispersed in 30 ml of organic solvents such as anhydrous ethanol, isopropyl alcohol and dimethylformamide (DMF) for 1 h (Figure 2.2). Thin graphene films were made by electrophoresis, floating method[86] and spray method. For electrophoresis, a voltage of DC 40 V was applied between two silicon or Al electrodes whose gap was 1 cm (Figure 2.3) in a dispersed graphene ethanol solution. Another graphene flakes film was prepared by a floating method. A graphene suspension (0.5 mL) in DMF was mixed with 40 mL of water and 4 mL of ethyl acetate (EA) was placed onto the aqueous mixture. After few minutes, a graphene film floating on aqueous phase was transferred onto fluorine-doped thin oxide (FTO) glass as counter electrode instead of Platinized electrode for dye-sensitized solar cell (DSSC) and dried at 100°C for 10 minutes to remove residual solvent.

For spray coating method, graphene suspension in DMF was sprayed on FTO (fluorine-doped thin oxide) glass repeatedly at 80°C with portable spray nozzle (Figure 2.4). DSSC devices were prepared as a general method. FTO plates were cleaned in a detergent solution using ultrasonic bath for 15 min and rinsed with water. Then they were cleaned again in ethanol for 10 min. To

prepare blocking layer, the FTO glass was spin-coated with 5 wt% of titanium di-isopropoxide bis(acetylacetonate) in butanol and then annealed at 450 ℃ for 1 hour. A transparent nanocrystalline layer on the FTO glass was coated by doctor blade technique, and then gradually annealed under an air at 450 ºC for 1 h. The $TiO_2$ films were immersed into a N719 (solaronix) dye solution in ethanol under heating to 50 ℃ for 12 h. Controlled Pt-counter-electrodes was prepared by coating with drop of $H_2PtCl_6$ solution (0.5 M in EtOH) on FTO glass and then sintered at 450 ℃ for 30 min. Graphene flakes-counter electrode was prepared by spray and floating method on FTO glass and then sintered at 350 ℃ for 1 hour. Dye absorbed $TiO_2$ electrode and counter electrodes were assembled into a sealed sandwitch-type cell using a 60 μm -thick surlyn. The composition of the electrolyte was as follows: 0.7 M of 1 butyl -3-methyl imidazolium iodide (BMII), 0.03 M of $I_2$, 0.1 M of guanidium thiocyanate (GSCN), and 0.5 M of 4 *tert*-butyl pyridine (TBP) in a mixture of acetonitrile and valeronitrile (85: 15 *v/v*). Graphene flakes was analyzed by using a scanning electron microscope (SEM; JEOL ltd. JSM6700F (10 kV)) and a high-resolution transmission electron microscope (JTEM; EOL, JEM-

3000F (300 kV)). UV-Vis spectra were recorded on a UV-3600 spectrophotometer (Scinco, NEOSYS-2000) and Raman spectroscopy. Raman spectra were observed by using a micro-Raman system equipped with a homemade sample stage, a monochrometer (SPEX 500 M), and a CCD camera cooled with liquid nitrogen (Roger Scientific 7346-001 Model). Raman spectra were observed by excitation with a 514.5 nm laser line. The incident laser power on the sample was approximately 100 μW, and the acquisition time was 100 s. Current density-voltage (J-V) characteristics of the DSSCs were measured using an electrometer (KEITHLEY 2400) under AM 1.5 illumination (100 $mW/cm^2$) provided by a solar simulator (1 KW xenon with AM 1.5 filter, PEC-L01, Peccel Technologies).

**Figure 2.2. An optical image of graphene suspension in DMF.**

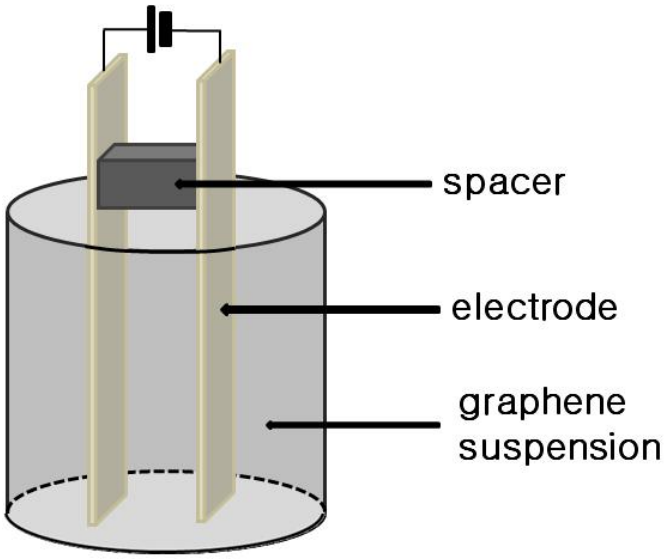


**Figure 2.3. A schematic of electrophoresis system.**

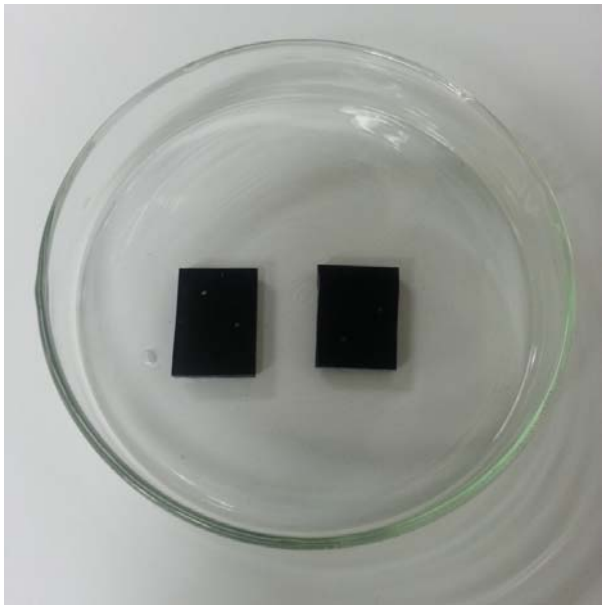

**Figure 2.4. A optical image of graphene flakes film on FTO glass by spray method.**

### 2.3. Fabrication of graphene flakes with tunable size and layer using a thermal plasma jet system

The thermal plasma jet system used here is basically the same one as reported.[77] Thermal plasma of Ar was generated by applying a high voltage of ~3 kV between a zirconium-containing tungsten cathode and a copper anode. The thermal plasma jet was stabilized by DC 180-210 A. The Ar plasma jet flowed into a Cu anode nozzle whose inner diameter was 6 mm, then we used an attached carbon tube (15 mm in inner diameter) to fabricate larger graphene flakes. A well polished graphite plate was placed in the path of the plasma gas flow, perpendicular to the attached carbon tube. The distance between the end of the attached carbon tube and the graphite plate was 10 cm. Ethanol was used as a carbon source and inserted continuously in thermal plasma jet inlet. The flow rates of ethanol, which was controlled by a syringe pump (Syringe Pump NE-1000), was 0.1 mL per min.

In addition, we developed a new method in injection rate controlled of carbon source for fabrication of thin layer graphene. Previous fabrication method of graphene flakes using thermal plasma jet was exfoliative method

from continuous collision between fixed graphite plate and carbon atomic beam. But in this method, we could not fabricate thin layer graphene flakes for increasing injection rate of carbon source. So we used a rotating graphite plate (2000 rpm) using motor replace of fixed graphite plate to prevent graphene flakes from thick-layer. In addition, we modified thermal plasma jet system that we installed another plasma torch to original thermal plasma system (Figure 2.5).

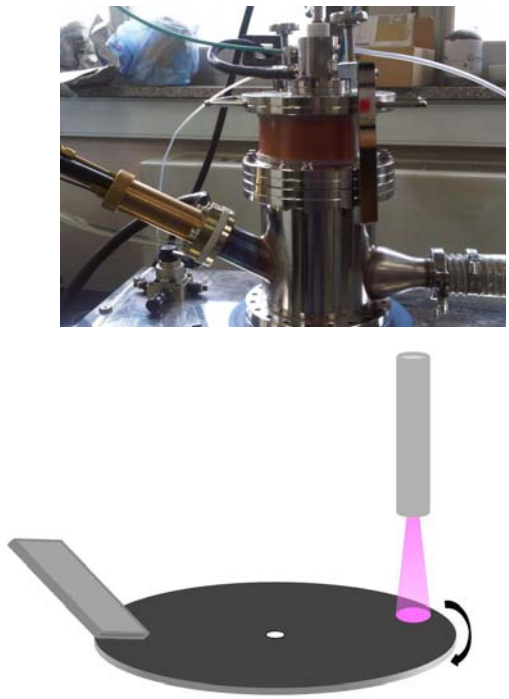

**Figure 2.5. Optical image of modified plasma system (up) and a schematic of rotating graphite plate (down).**

As shown Figure 2.5 the carbon atomic beam and another plasma beam generate each collision spots on graphite plate. This method is to produce the clear surface of graphite plate and to be able to peel off graphene flakes from graphite plate easily. In this experiment, ethanol (0.2 ml/min) and methane gas(400~ 700 sccm) were used as the carbon sources, and the attached carbon tube of internal diameter 0.5cm and length 20nm was placed at distance of 10cm from the carbon tube to graphite plate. Another carbon tube (0.2cm X 1.5cm of nozzle shape) used in the exfoliative plasma torch was very closely located to graphite plate. The plasma beam was stabilized under 350 A. Produced graphene flakes soot was harvested through a wall of thermal plasma chamber. Graphene flakes were analyzed by using a scanning electron microscope (SEM; JEOL ltd. JSM6700F (10 kV)) and a high-resolution transmission electron microscope (JEOL, JEM-3000F 300 kV).

## 2.4. Size-controllable and low-cost fabrication of graphene quantum dots using thermal plasma jet system

The thermal plasma jet system used here is basically the same one as reported,[77] but no graphite plate was placed in the path of the plasma gas, nor was a catalyst source injected (Figure 2.6). A non-transferred thermal plasma system was operated by a direct current. Ar gas (99.999%) was used as a plasma gas and the flow rates of Ar gas, which was controlled by mass flow controller (DFC-4000, Flow Tech Co.) was 13.5 ksccm. Thermal plasma of Ar was generated by applying a high voltage of ~3 kV between a zirconium-containing tungsten cathode and a copper anode. The thermal plasma jet was stabilized by DC 210-300 A. The Ar plasma jet flowed into a Cu anode nozzle whose inner diameter was 6 mm, then continued through an attached carbon tube (10 mm in inner diameter and 50~200 mm in length). Ethylene gas was used as a carbon source and inserted continuously in thermal plasma jet inlet. The flow rates of Ethylene gas, which was controlled by a mass flow controller, was 2500 mL per min. Produced carbon soot was harvested through a wall of thermal plasma chamber. Carbon soot produced was

dispersed in ethanol by stirring with a stirring rod. In this case, isolated GQDs were dispersed in ethanol. GQDs were analyzed by using a scanning electron microscope (SEM; JEOL ltd. JSM6700F (10 kV)) and a high-resolution transmission electron microscope (JEOL, JEM-3000F (300 kV)). UV-Vis spectra were recorded on a UV-3600 spectrophotometer (Scinco, NEOSYS-2000). X-ray photoelectron spectroscopy (XPS) was performed to determine the composition of our GQDs. Raman spectra were observed by using a micro-Raman system equipped with a homemade sample stage, a monochrometer (SPEX 500 M), and a CCD camera cooled with liquid nitrogen (Roger Scientific 7346-001 Model). Raman spectra were observed by excitation with a 514.5 nm laser line. The incident laser power on the sample was approximately 100 μW, and the acquisition time was 100 s. AFM images were taken using a PSIA (XE-150) atomic force microscope. PL and PLE spectra were obtained using a homemade spectrophotometer. Absolute quantum yield was measured by absolute PL quantum yield measurement system QE-1200 (Otsuka Electronics).

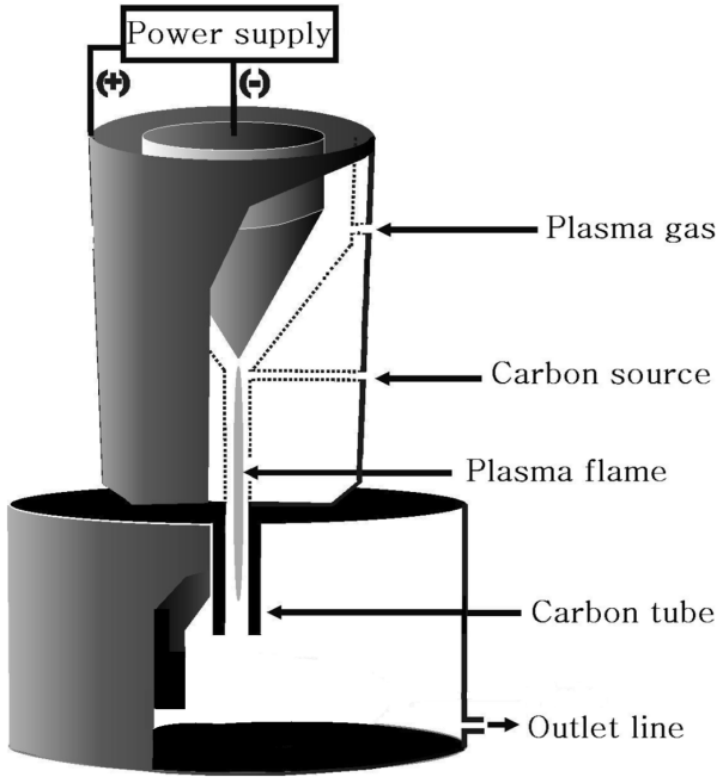


**Figure 2. 6. A schematic of the thermal plasma jet system for the production of GQDs**

## CHAPTER 3. Fabrication of graphene flakes using a thermal plasma jet system

SEM images of graphene flakes composed of multi-layer graphene sheets fabricated by injecting ethanol as a carbon source into the thermal plasma jet system are shown in Figure 3.1. It should be mentioned that any gaseous or liquid hydrocarbons or alcohols could be used as a carbon source. In the low-magnification image, many graphene sheets are agglomerated into flakes that form a cauliflower-like appearance. In the high-magnification image, each graphene sheet is clearly visible. Most graphene sheets, even those in the back, are visible. This means that the graphene sheets are thin and transparent. Graphene is very pure and, as such, no impurities like amorphous carbon or carbon nanotubes are seen. In the fabrication, a carbon tube with a length of 20 cm and inner diameter of 0.5 cm was attached at the end of the anode. A graphite plate was placed 10 cm away from the end of the attached carbon tube. The injection rate of ethanol was 0.1 mL/min. A sample for the SEM images was collected on the wall surface of the reaction chamber, which was approximately 9 cm away laterally from the spot that was hit by the plasma

gas on the graphite plate. The temperature at the graphite plate was approximately 1000 K. When 3.00 mL (2.37 g) of ethanol was injected, approximately 0.100 g of graphene was fabricated. The yield of graphene from the carbon mass of ethanol is approximately 8 %. Most of the graphene sheets were collected on the wall surface and at the bottom of the chamber, and a few were collected on the Teflon filter (0.2 μm in pore size) that was set on the exit hole.

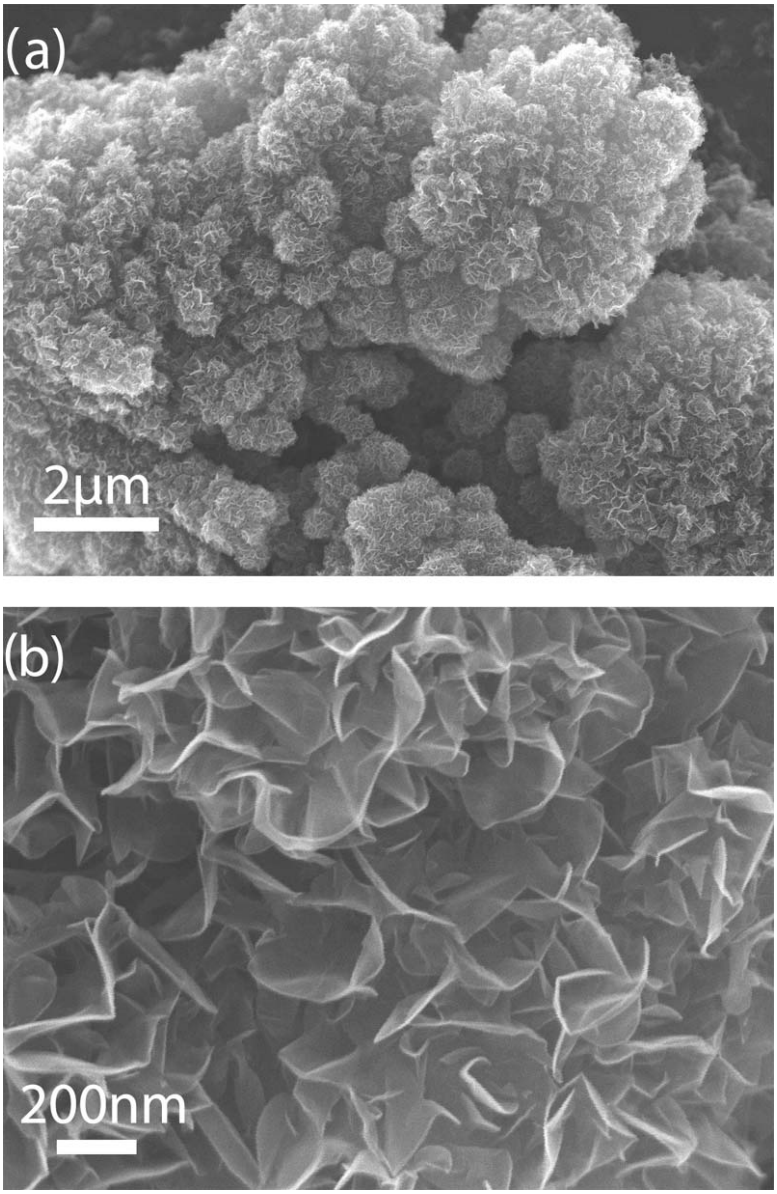


**Figure 3.1. SEM images of multi-layer graphene sheets produced by injecting ethanol continuously (0.1 mL/min) into an Ar plasma jet: (a) low and (b) high magnifications.**

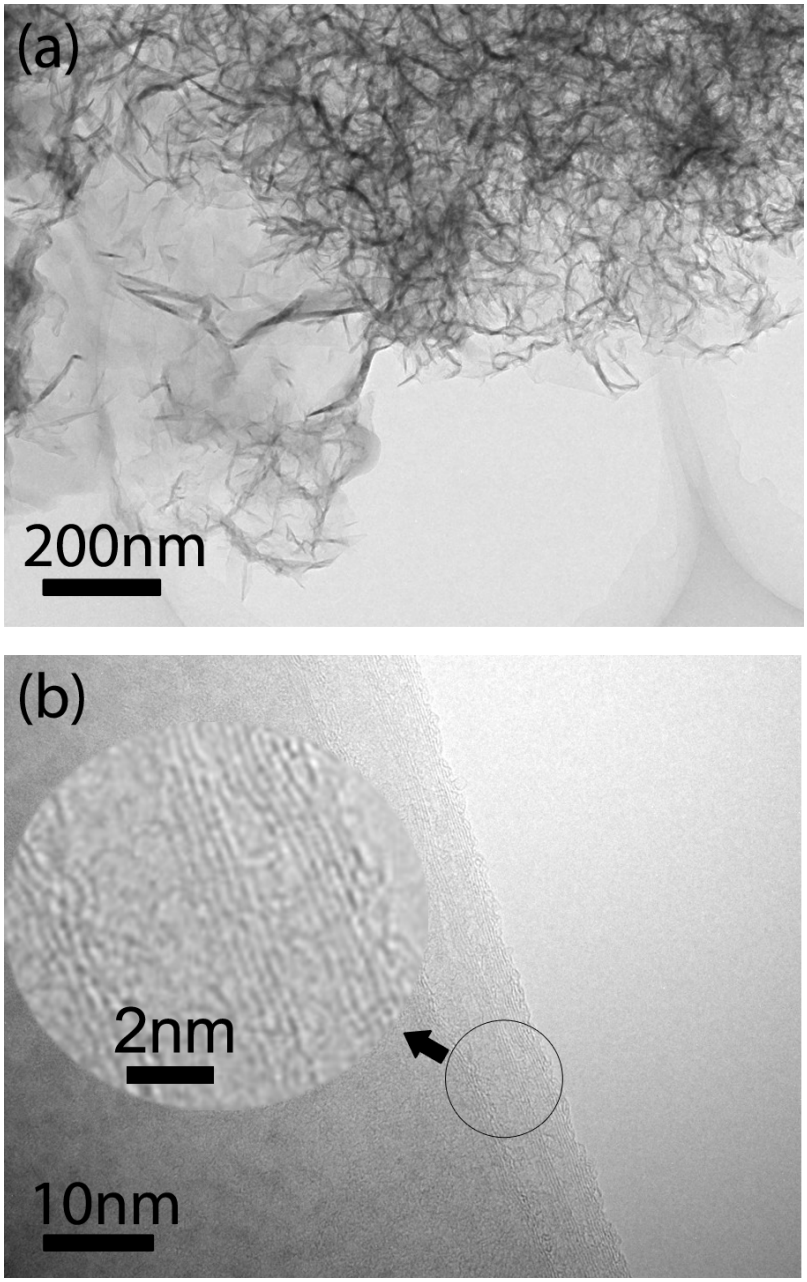


**Figure 3.2. TEM images of graphene sheets fabricated: (a) low and (b) high magnifications.**

In Figure 3.2, the low- and high- magnification TEM images of the graphene sheets fabricated are shown. In the low-magnification image, many graphene sheets overlap one other with the exception of some edges. In the preparation of the TEM sample, we added a very small number of graphene sheets into ethanol, dispersed them by manual agitation, and then applied and dried one drop of the dispersed solution on a TEM grid. In order to retain the original shape of graphene sheets, we did not sonicate the solution. In the high-magnification image that was observed at an edge, some fringes were seen. In Figure 3.2(b), there are three series of fringes. Two series are clear while the other one is relatively unclear. The number of fringes in each series is in the range of 3 - 5. Most edges of the thin graphene sheets are slightly folded (Figure 3.1.). For the folded graphene sheets, fringes could be observed like the fringes of the walls of carbon nanotubes. The gap between the fringes is approximately 0.33 nm and is in agreement with the reported value.[69] It should be mentioned that the gap between the fringes of multi-walled carbon nanotubes also has the same value.[75] For multi-walled carbon nanotubes, the space between two series of the fringes must be uniform through the entire length. However, the space between the series of the fringes in Figure 3.2(b) is not uniform. This is strong evidence that the fringes are not due to carbon nanotubes. For thick graphene sheets, edges were not folded and no fringes were observed.

In Figure 3.3, three kinds of graphene sheets are shown: one is very

transparent and the other two are not. The thicknesses of the relatively opaque sheets were different from the transparent one. They were synthesized under the same conditions, but their ethanol injection rates were different. The injection rate of ethanol was 0.10, 0.15, and 0.20 mL/min for graphene in Figure 3.3(a)-(c) respectively. It is concluded that the thickness of graphene sheets increases with increasing ethanol injection rate under the same conditions.

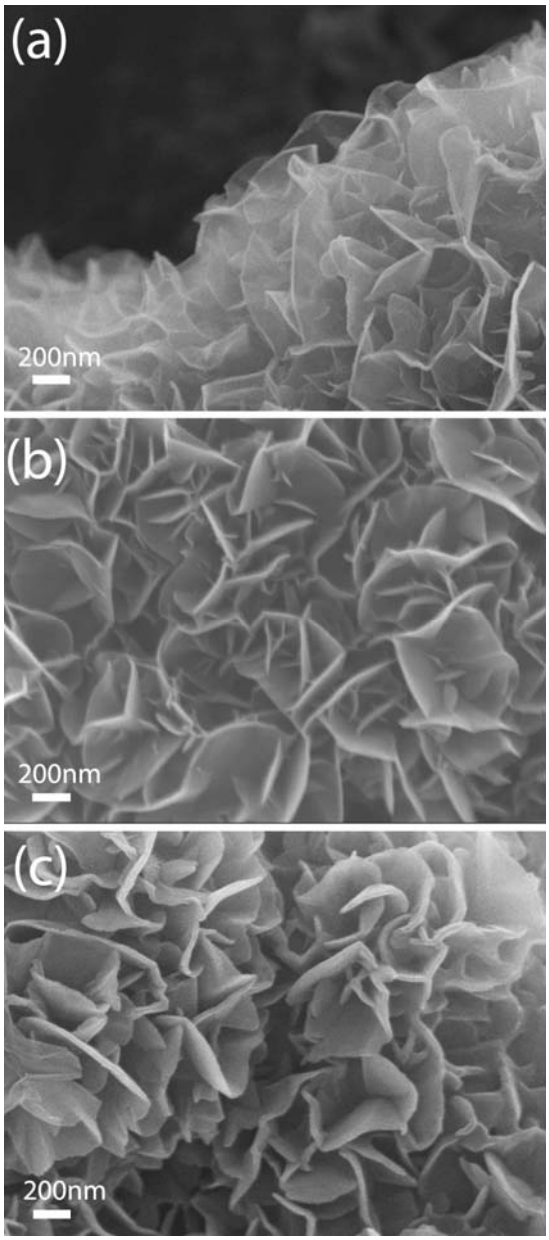


**Figure 3. 3. Graphene sheets fabricated with different ethanol injection rates. The injection rates of ethanol were (a) 0.10, (b) 0.15, and (c) 0.20 mL/min.**

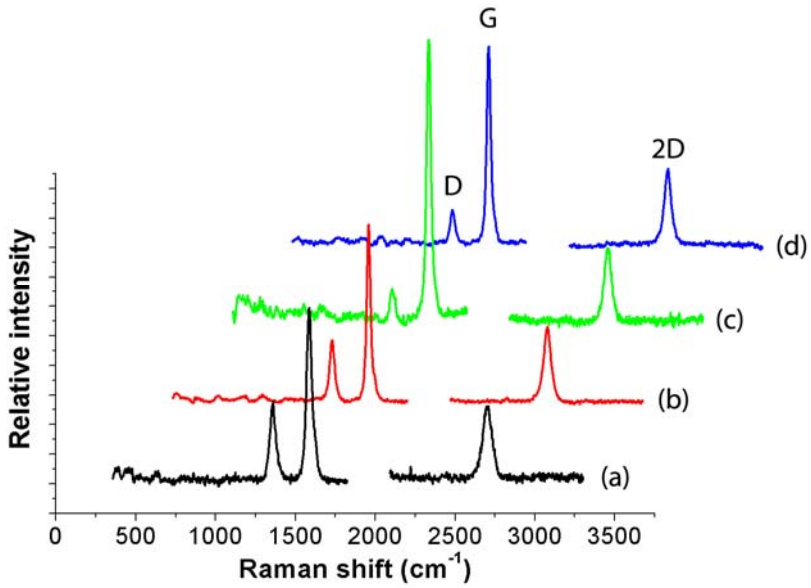


**Figure 3.4. Raman spectra of graphene sheets fabricated under different conditions, measured by excitation with a 514.5 nm Ar ion laser line. A carbon tube [(a)-(c) 20 and (d) 26 cm in length, and 0.5 cm in inner diameter] was attached at the end of the anode and a graphite plate was placed (a)-(c) 10 and (d) 4 cm away from the end of the attached carbon tube. The injecting rates of ethanol were (a) 0.1, (b) 0.15, (c) 0.2, and (d) 0.1 mL/min. The relative intensities were scaled to have similar heights for the 2D peak at ~2710 $cm^{-1}$.**

Raman spectroscopy has been used to characterize the crystalline structure of graphene produced. Figure 3.4 shows the Raman spectra of the graphene fabricated under different conditions, measured by excitation with a 514.5 nm laser line. The relative intensities were scaled to have similar heights for the 2D peak at ~2710 $cm^{-1}$. The samples for Figure 3.4(a)-(c) were fabricated by attaching a 20 cm carbon tube, while a 26 cm tube was attached for Figure 3.4(d). The distance between the end of the attached carbon tube and the graphite plate was 10 cm for (a)-(c), and 4 cm for (d). The ethanol injecting rate was (a) 0.1, (b) 0.15, (c) 0.2, and (d) 0.1 mL/min. The SEM images of graphene fabricated under the same conditions for the samples for Figure 3.4(a)-(c) are shown in Figure 3.3. It should be mentioned that the SEM image of the graphene sample for Figure 3.4(d) was almost the same as the one shown in Figure 3.3(a). In Raman spectra, there are three distinct peaks. The peak near 2710 $cm^{-1}$ is the 2D peak of graphene. The position and shape of the 2D peak has been used to distinguish between single-layer, double-layer, and multi-layer graphene.[78] For single-layer graphene sheets, the peak is very sharp and appears at a Raman shift lower than 2700 $cm^{-1}$. For double-layer

sheets, upon 514.5 nm excitation, the peak is located near 2700 $cm^{-1}$, and near 2715 $cm^{-1}$ for five-layer sheets.[78] It should be mentioned that the Raman peak positions of graphene are altered by the excitation wavelength.[78] As the number of layers was increased, the peak usually broadens and the peak position shifts up.[78] In the Raman spectra of Figure 3.4, the 2D peak is near (a) 2708, (b) 2709, (c) 2710, and (d) 2708 $cm^{-1}$. There are no significant differences between the 2D peak positions. By the Raman data reported[78], our graphene sheets may have three or four layers. However, by the SEM images, our sheets show a very different appearance with respect to thickness (Figure 3.3). The G peak of graphene sheets is observed at ~ 1580 $cm^{-1}$.[78] For graphite oxide sheets, this peak broadens and shifts to 1594 $cm^{-1}$.[79] The G peak of the fabricated sheets is very sharp and located at approximately 1586 $cm^{-1}$, which shows that oxygen from the ethanol precursor was not present on the graphene sheets. The relative intensity between the G and 2D peaks changes with the number of layer of graphene sheets.[17,19] The intensity of the G peak is weaker than that of the 2D peak for single-layer graphene, while it is stronger for double- and multi-layer graphene.[17,19] The largest G/2D

intensity ratio is observed in the Raman spectrum of Figure 3.4(c). This may mean that the graphene sheets for the sample in Figure 3.4(c) have the thickest layers. The SEM images shown in Figure 3.3 support this suggestion. These sheets were fabricated by injecting ethanol with the highest rate: 0.2 mL/min.

The D peak near 1359 $cm^{-1}$ is known due to the presence of structural disorders in graphene sheets[78]. For highly oriented pyrolytic graphite (HOPG), this band disappears.[80] Therefore, the G/D intensity ratio can be used to figure out the crystallinity of graphene. A higher ratio indicates that a better graphene crystallinity. However, the edges of graphene sheets are always seen as defects. Our graphene sheets are agglomerated randomly, and the edges could contribute significantly to the Raman signals. In Figure 3.4(a)-(d), the ratio is approximately (a) 2.1, (b) 2.9, (c) 8.5, and (d) 5.9. For Figure 3.4(a)-(c), the ratio increases with increasing ethanol injection rate. Under the same fabrication conditions, the crystalline structure of graphene sheets made would improve by increasing the injection rate of ethanol. The reason for this improvement will be discussed later. There were no significant differences between the samples for Figure 3.4(a) and (d) in their SEM and TEM images.

However, their G/D intensity ratios are very different. This means that two kinds of graphene sheets fabricated under different conditions may have significantly different crystalline structure. For the reported graphene flakes, the G/D intensity ratio is less than 2.[78] Our graphene sheets fabricated at optimum conditions show a much larger G/D intensity ratio than the reported graphene flakes. This large difference between the G/D intensity ratios may suggest that our graphene sheets may have a better crystalline structure than any reported graphene sheets of the flake type.

In our synthesis of graphene sheets, the carbon tube attached and the graphite plate have very important roles. No graphene was made when a Si plate was placed instead of a graphite plate. This means that graphene is made by an epitaxial growth on graphite. Since an epitaxial growth takes place, the surface crystalline structure of the graphite plate will affect the crystalline structure of the graphene fabricated. The attached carbon tube may somewhat reduce the kinetic energy of the atomic beam. Ethanol is atomized by the thermal energy of Ar plasma, which has a very high temperature (~ 10000 K).[79] Atoms, including Ar, flow at a very high speed through the anode nozzle

and the attached carbon tube to form an atomic beam. The kinetic energy of the atomic beam, including carbon atoms, may be slightly reduced during its flow through the carbon tube. It should be mentioned that when the graphite plate is placed very close to the anode without attaching a carbon tube, carbon nanotubes are made at the spot that was directly hit by the plasma flame on the graphite plate, while amorphous carbon is made on the other places[82]. This means that graphene is not made when carbon atoms collide on the graphite plate with a relatively high energy. Therefore, it is concluded that graphene sheets are made by an epitaxial growth when a carbon atomic beam, having a proper energy, collides with a graphite plate. In addition to reducing the kinetic energy of the atomic beam, another important role of the attached carbon tube is to make a homogeneous flow of gases. The atoms including carbon in the atomic beam will collide with each other and to the inner surface of the attached carbon tube during their flow. They will gradually become homogeneous during their flow through the carbon tube. The crystalline structure of the graphene sheets fabricated may be affected by the homogeneity of the carbon atomic beam.

The distance between the graphite plate and the end of the attached carbon tube is a critical factor in the synthesis process. The kinetic energy of the atomic beam may be reduced greatly during its flow to the graphite plate, after passing the end of the attached carbon tube. Also, the atomic beam will disperse laterally during its flow to the graphite plate. Therefore, the distance between carbon atoms in the lateral direction will increase continuously during flow to the graphite plate after passing the end of the carbon tube. Since graphene sheets are made by an epitaxial growth, the lateral distance between carbon atoms colliding almost simultaneously to the graphite plate will affect the crystalline structure of the graphene sheets fabricated. The results shown in Figure 3.4(a) and (d) may show evidence that the crystalline structure of the graphene sheets fabricated is critically affected by the distance between the graphite plate and the end of the carbon tube. When the injection rate of ethanol was increased under the same experimental conditions, the crystalline structure of graphene sheets was improved based on the increase of the G/D intensity ratio (Figure 3.4(a)-(c)). By increasing the injection rate, more carbon atoms will collide simultaneously to the graphite plate. This may

have two effects. First, the number of layers of the graphene sheets made increases. Also, the number of defects - such as voids - formed on each layer of the graphene sheets will decrease. The increase in simultaneous collisions decreases the number of voids formed on each layer, resulting in the increased G/D intensity ratio. There are several factors that affect the crystalline structure of graphene sheets fabricated: the injecting rate of ethanol; the length and diameter of the carbon tube attached; the distance between the graphite plate and the end of the carbon tube attached; and the surface structure of the graphite plate. When these factors are optimized simultaneously, graphene sheets having a very good crystalline structure could be fabricated. The factors affecting the crystalline structure of graphene sheets fabricated should be studied in detail.

Previously, we have demonstrated that the number of layers of graphene sheets could be controlled roughly by controlling the rate of ethanol injection. The number of carbon atoms colliding with the graphite plate per second will be proportional to the injection rate of ethanol. The number of layers will increase when carbon atoms collide with graphene sheets and form new layers

on them. New layers will be formed until the graphene sheets leave the reaction zone. By controlling both the time of the graphene sheets dwelling in the reaction zone and the ethanol injection rate, the number of layers can be precisely controlled. However, we currently have no method to control the time of the graphene sheets dwelling in the reaction zone. In addition, only multi-layer graphene sheets can be fabricated. If we could find a method to control the sheets' dwelling time in the reaction zone, we could consequently control the number of layers of graphene sheets more precisely. If this were achieved, we could even fabricate single-layer graphene sheets. We could also increase the production rate of graphene sheets. Using our present technique, the production rate of graphene sheets is relatively low because we must limit the ethanol injection rate to about 0.1 mL/min. Were we to significantly increase the injection rate, the number of layers begins to increase instead of increasing the production rate. If we could immediately strip off the graphene sheets from the reaction zone after formation, the dwelling time in the reaction zone would decrease markedly. This decrease in dwelling time would increase the graphene sheet production rate without increasing the layer count.

If we want to further increase production rate, we must decrease the formation time. The formation time can be reduced by increasing the colliding rate of carbon atoms to the graphite plate; the colliding rate can be increased by increasing the injection rate of ethanol. By this logic, the production rate of graphene sheets will increase by increasing ethanol injection rate and by controlling dwelling time. If these could be achieved, mass production could also be achieved, since our method is a continuous process with a relatively high yield (~8%).

In summary, We have developed a method to fabricate graphene flakes composed of high-quality multi-layer graphene sheets using a thermal plasma system. Graphene sheets are made by an epitaxial growth on a graphite plate when a carbon atomic beam, generated by continuously injecting ethanol into the Ar plasma, collides with the graphite plate after flowing through a carbon tube attached to the anode. The graphene sheets made are scattered by the force of the plasma gas colliding to the plate. The graphene sheets fabricated are very pure and show a relatively good crystalline structure. The number of layers of graphene sheets could be controlled by controlling the rate of ethanol

injection. The yield of our process is approximately 8% and this process is continuous.

## CHAPTER 4. Fabrication of dispersible graphene in organic solvents using thermal plasma jet system

The TEM images of graphene produced are shown in Figure 4.1. The TEM sample was prepared by dropping carbon soot solution that had dispersed in ethanol by sonication, on a TEM grid. The raw carbon soot produced was well dispersed in ethanol by sonication, and the dispersed solution was very stable for several months. In low magnification image, one can see lots of small size graphene that are folded and overlapped one other with the exception of some edges. It was not easy to measure the average size of graphene precisely because most graphene was folded and overlapped one other. By our rough estimation, the average size was about 100 nm. From the high resolution TEM image, one can see fringes that could be observed from folded graphene. The edge of the folded graphene is very similar to the edge of carbon nanotubes. For carbon nanotubes the number of fringes corresponds to that of walls. However, for graphene the number of fringes corresponds to the number of graphene layers. In Figure 4.1(b), one can see several graphene fringes. The number of fringes is found in the range of 1-3. For the longest edge in the

Figure 4.1 (b), 3 fringes are clearly seen. Besides graphene, some onion type materials, whose fringes look like contour lines, are also observed. Onion type materials are much smaller than graphene in size. Their size is about 10 nm. These onion type carbon materials might be made by a gas phase reaction.

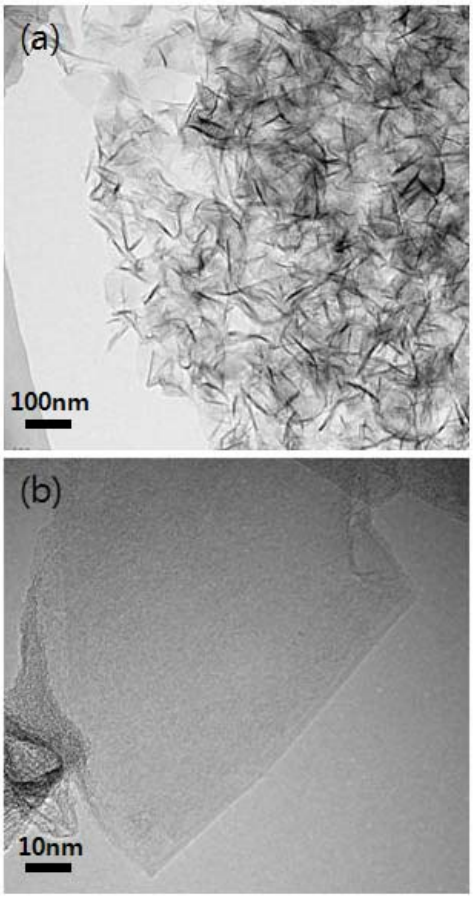


**Figure 4.1. Low and high magnification TEM images of graphene produced by injecting ethylene continuously (500 sccm) into an Ar plasma jet.**

In our fabrication method, carbon atoms are generated continuously by thermal decomposition of carbon source, and they form an atomic beam. The

beam then flows through a carbon tube (20 cm in length and 0.5 cm in inner diameter) attached to the anode. Without placing a graphite plate in the path of the beam, no graphene was made. Therefore, graphene might be made by epitaxial growth where a carbon atomic beam, having the proper energy, collided with a graphite plate that was placed in the path of the beam, perpendicular to the attached carbon tube. The graphene made on the graphite plate was scattered by the colliding force of Ar atoms. With injecting ethylene as a speed of 500 sccm, the production rate of graphene based on the collected carbon soot amount was about 1.5 g/h. The formation mechanism of onion type materials might be different from that of graphene because no onion type carbon materials were made when the injection rate of carbon source was relatively low. In the previous report,[77] the injection rate of ethanol was 0.1 mL/min, corresponding to about 39 sccm in gas phase at room temperature, and no onion type carbon materials were made. The injection rate of Ar plasma gas was 13.5 L/min, while that of ethylene was 0.5 L/min (500 sccm). When one molecule of ethylene is decomposed, two carbon atoms are generated. Therefore, the percent of carbon atoms might be high enough to take place collision reactions between carbon atoms during flowing through the attached carbon tube, and onion type materials might be formed by a gas phase reaction.

UV-visible absorption spectrum of graphene dispersion in ethanol is shown in Figure 4.2. Photographs of graphene dispersions in ethanol are shown as

inserts. Although carbon soot, which was mostly graphene, was well dispersed in ethanol by sonication, in water very small portion was dispersed even by sonication. The graphene suspension shows strong optical absorption in the UV region (230–320 nm), with a tail extending into the visible range. No PL emission peak was observed in visible region from our graphene. The size of our graphene is about 100 nm, which may be too large to have a band gap corresponding to visible lights by quantum confinement[55].

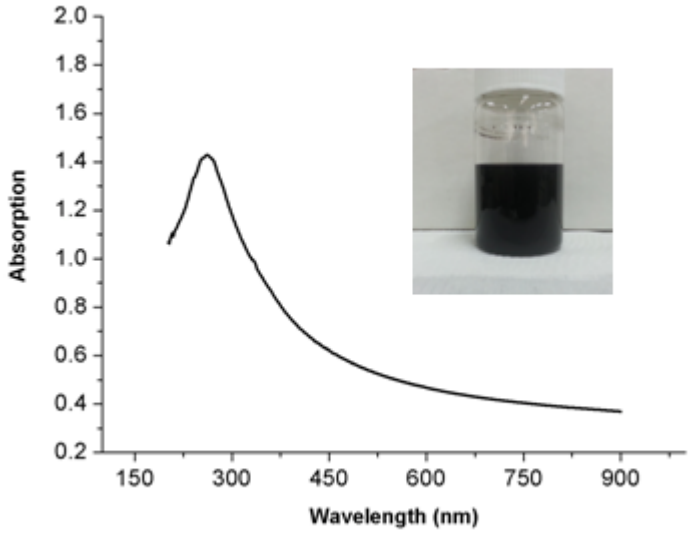


**Figure 4.2. UV-visible absorption spectrum of carbon soot dispersed in ethanol. Photographs of graphene dispersions ethanol are shown as inserts**

The SEM images of graphene flakes deposited on Al plates by

electrophoresis are shown in Figure 4.3. In electrophoresis, we applied a voltage of DC 40 V between two Al plates, whose gap was 1 cm, in the graphene dispersed ethanol solution. We added small amount of water to increase conductivity. With increasing the time of electrophoresis, more graphene was deposited. For the case of 7 min electrophoresis, one can see that the surface is almost completely covered with graphene. The size and shape of graphene are not uniform. Graphene was deposited on the surface of the ( – ) electrode.

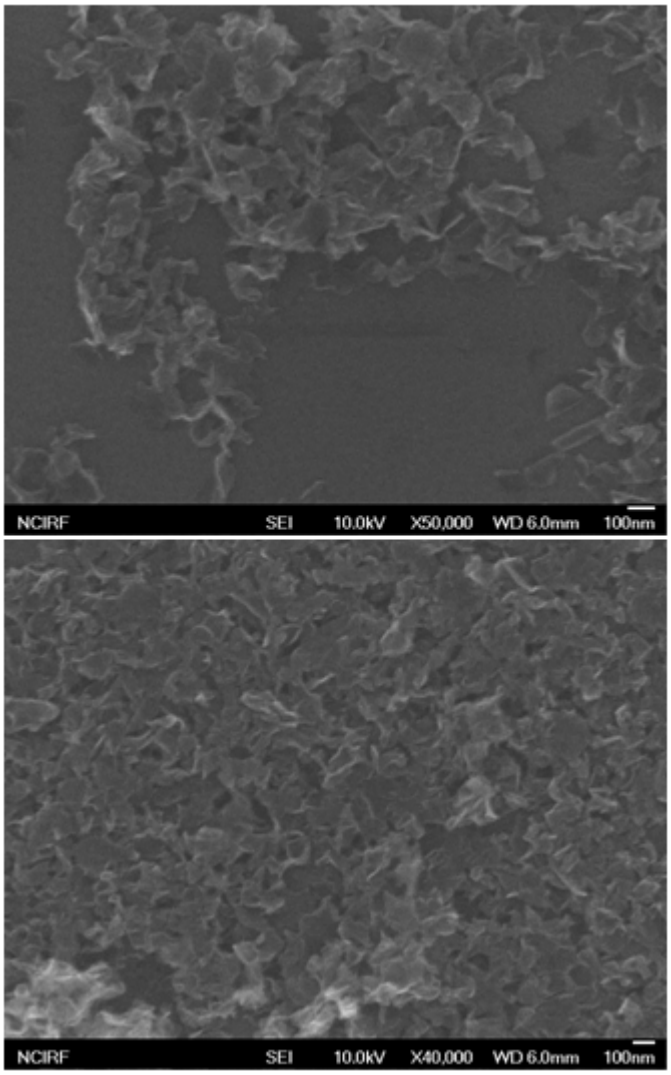


**Figure 4.3. SEM images of graphene flakes deposited on Al plates by electrophoresis. Electrophoresis was done in a graphene dispersed ethanol solution by applying a voltage of DC 40 V. The counter electrode was also Al, and the gap between electrodes was 1 cm. The electrophoresis time was (a) 2 min and (b) 7 min.**

The SEM images of graphene flakes deposited on FTO glass by spray method and floating method are shown in Figure 4.4. In Figure 4.4, uniform graphene assembled film consisting of closely packed pristine graphene flakes.

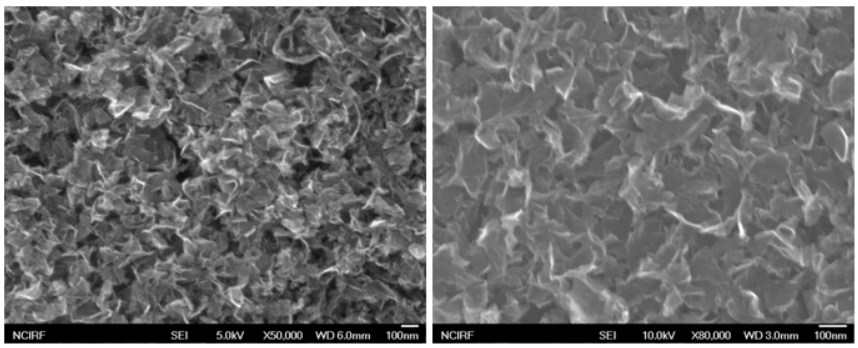


**Figure 4.4. SEM images of graphene flakes deposited on FTO glass by spray method (left) and floating method (right).**

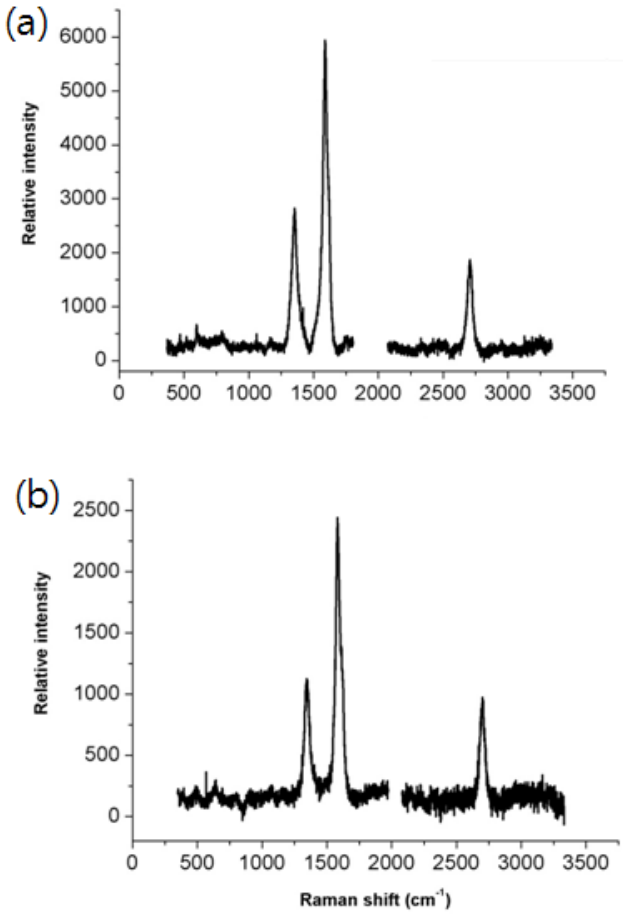


**Figure 4.5. Raman spectra of (a) a graphene film prepared by electrophoresis and (b) raw carbon soot powder.**

The Raman spectrum measured from a graphene film prepared by electrophoresis is shown in Figure 4.5. There are three typical graphene peaks; the D peak near 1360 $cm^{-1}$, G peak near 1594 $cm^{-1}$ and 2D near 2703 $cm^{-1}$. The G peak is due to the $E_{2g}$ vibrational mode, and the 2D band is a second-order two-phonon mode. The D peak is known due to the presence of structural disorders in graphene sheets.[78] The position and shape of the 2D peak has been used to distinguish between single-layer, double-layer, and multi-layer graphene.[78] For single-layer graphene sheets, the peak is very sharp and appears at a Raman shift lower than 2700 $cm^{-1}$. For double-layer sheets, upon 514.5 nm excitation, the peak is located near 2700 $cm^{-1}$, and near 2715 $cm^{-1}$ for five-layer sheets.[78] It should be mentioned that the Raman peak positions of graphene are altered by the excitation wavelength[78]. As the number of layers increases, the peak usually broadens and the peak position shifts up.[78] The position of 2D peak is near 2703 $cm^{-1}$. This may mean that our graphene may have two or three layers. This result is well agreed with TEM observations. The D band is not Raman active for pristine graphene like oriented pyrolytic graphite (HOPG) but can be observed where symmetry is

broken by edges or in samples with a high density of defects. Therefore, the G/D intensity ratio can be used to figure out the crystallinity of graphene. A higher ratio indicates better graphene crystallinity. In the spectrum, the intensity of D peak is relatively strong compared to that of G peak. However, the edges of graphene sheets are always seen as defects. Therefore, the G/D intensity ratio does not simply represent the crystallinity of our graphene flakes. In the photocurrent density-voltage (J-V) curve of DSSCs employing the graphene flakes electrode and controlled Pt electrode is shown in Figure 4.6. Details of the photovoltaic characteristics are listed in Table 4.1. The DSSC with a typical Pt electrode had a short-circuit current density ($J_{sc}$) of 11.09 mA/cm2, an open circuit voltage ($V_{oc}$) of 0.82 V a fill factor (FF) of 0.73%, and a photo conversion efficiency (η) of 6.61%. The DSSC employing the floated graphene electrode showed better efficiency than sprayed graphene electrode. The average value of floated graphene electrode devices showed a short-circuit current density ($J_{sc}$) of 12.13 mA /cm2, an open-circuit voltage ($V_{oc}$) of 0.81 V and a fill factor (FF) of 0.63% and an photo conversion efficiency (η) of 6.21% while sprayed graphene electrode devices showed

11.62 mA/cm2, 0.81 V, 0.63% and 5.90%, respectively.

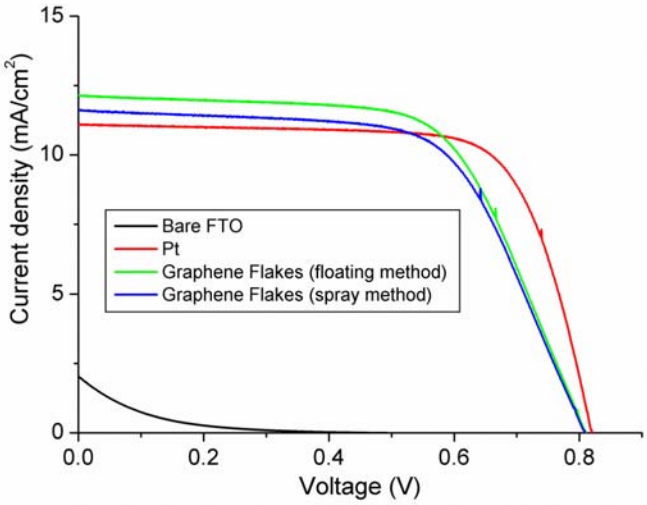


**Figure.4.6. The photocurrent density-voltage (J-V) curve of DSSCs employing the graphene electrode and controlled Pt electrode**.

| Counter electrode | $V_{oc}$ (v) | $J_{sc}$ (mA/cm$^2$ ) | FF | η( % ) |
|---|---|---|---|---|
| Bare FTO | 0.46 | 2.04 | 0.08 | 0.07 |
| Pt ( reference ) | 0.82 | 11.09 | 0.73 | 6.61 |
| Graphene flakes (floating method ) | 0.81 | 12.14 | 0.63 | 6.21 |
| Graphene flakes ( spraymethod ) | 0.81 | 11.62 | 0.63 | 5.90 |

**Table 4.1. Current density-voltage (J-V) characteristics of the DSSCs were measured using an electrometer (KEITHLEY 2400) under AM 1.5 illumination (100 mW/cm2) provided by a solar simulator (1 KW xenon with AM 1.5 filter, PEC-L01, Peccel Technologies).**

The Voc value of the DSSC based on the pt electrode and graphene electrode were almost the same, while $J_{sc}$ value of the device employed the graphene was higer than a conventional device. The enhanced $J_{sc}$ is attributed to the high electron transfer at the interface of electrolyte/counter electrode, resulting from high conductivity of graphene. In other words, improved catalytic ability helps iodide couple to react in the redox electrolyte.[87,88] From these result, the photo conversion efficiency of the DSSC based on our graphene electrode reached about 94% of that of the reference.

In summary, we have fabricated graphene, which is dispersible in organic solvents by sonication, by using thermal plasma system. We could make graphene flakes thin films by electrophoresis, spray and floating method in its dispersed solution. The dispersible property of our graphene flakes in organic solvents will have some merits in applications such as solar cell, composite material, barrier materials and electric device.

## CHAPTER 5. Fabrication of graphene flakes with tunable layer and size using a thermal plasma jet system

SEM images of graphene flakes composed of multi-layer graphene sheets fabricated with different inner diameter of attached carbon tube by injecting ethanol as a carbon source into the thermal plasma jet system are shown in Figure 5.1. The inner diameter of carbon tube was 5 and 15 mm for graphene in Figure 5.1 (a), (b) respectively. Figure 5.1 shows that the size of graphene flakes is approximately 300~500 nm for 5 mm inner diameter of carbon tube whereas for 15 mm inner diameter carbon tube, the size of graphene flakes is approximately 1.5~2 μm. It is concluded that the size of graphene flakes increases with increasing inner diameter of attached carbon tube under the same conditions.

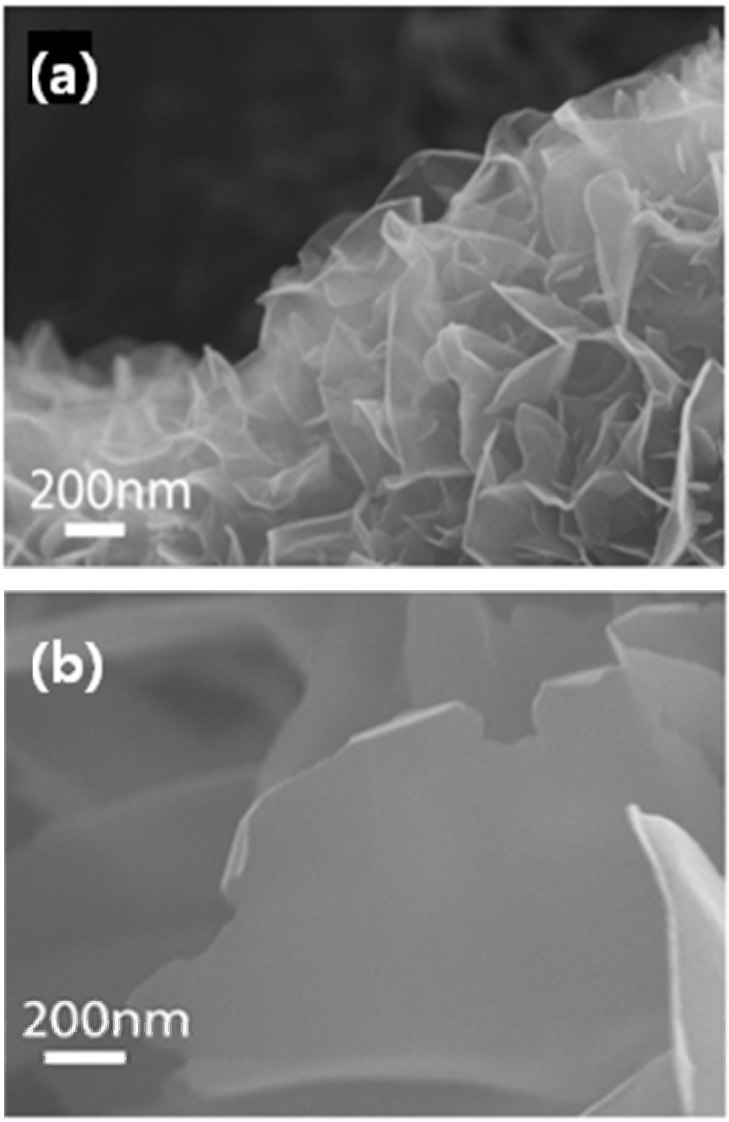


**Figure 5.5. Graphene sheets fabricated with different carbon tube inner diameter. The inner diameter of carbon tube (a) 5 and (b) 15 mm.**

In Figure 5.2, two kinds of graphene flakes are shown: one is very transparent and another is not. The thicknesses of the relatively opaque sheets were different from the transparent one. They were synthesized under the

same conditions (inner diameter and length of attached carbon tube, injection rate of carbon source and the distance between the end of the attached carbon tube and the graphite plate), but their graphite plate and plasma torch were different. For Figure 5.2 (a), graphene flakes were fabricated by previous method that graphene flakes using thermal plasma jet was exfoliative method from continuous collision between fixed graphite plate and carbon atomic beam. However, for Figure 5.2 (b), we used a rotating graphite plate (2000 rpm) using motor replace of fixed graphite. Furthermore, we modified thermal plasma jet system that we installed another plasma torch to original thermal plasma system to produce the clear surface of graphite plate and to be able to peel off graphene flakes from graphite plate easily. As a result of, we can prepare thin graphene flakes for increasing ethanol injection by using rotating graphite plate and additional plasma torch.

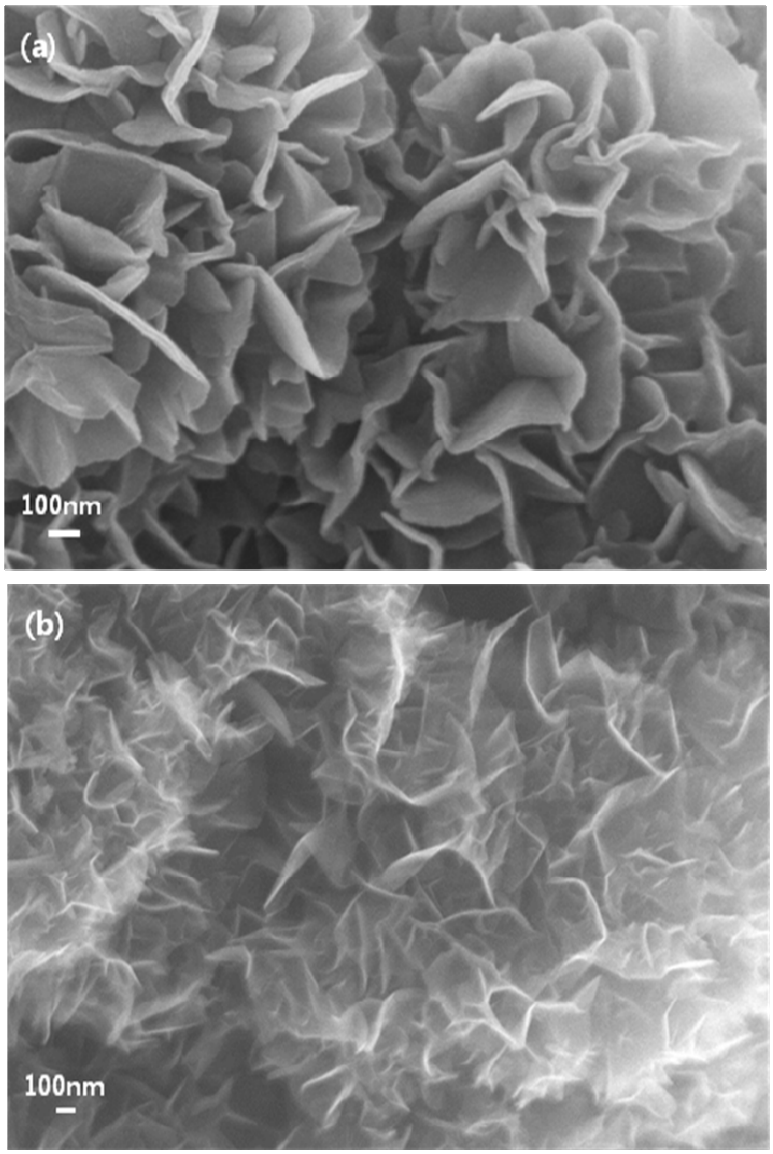


**Figure 5.2. (a) Ethanol (0.2 mL/min) was inserted plasma system with fixed graphite plate and single plasma torch. (b) Ethanol (0.2 mL/min) was inserted plasma system with rotating graphite plate and additional plasma torch**.

Also, methane gas was inserted continuously (400 ~700 sccm) as a carbon source into the plasma system to increase production rate of graphene flakes.

But there is a problem that the injection rate of carbon source and the layer of graphene flakes are in direct proportion to each other so, we used rotating graphite plate and installed another plasma torch to prevent graphene flakes from thick-layer. The results are shown in Figure 5.3. For the injection rate of methane gas was 400 sccm with fixed graphite plate, we can't fabricate a grapheen flakes. There are some impurities such as amorphous carbon and carbon-lumps instead of graphene flakes (Figure 5.3 (a)). However, for using rotating graphite plate and additional torch, graphene flakes were observed in Figure 5.3 (b). These are very transparent and there aren't impurities such as amorphous carbon. In Figure 5.4, the high- magnification TEM images of the graphene flakes fabricated with rotating graphite plate and additional plasma torch are shown. The number of fringes in graphene flakes is 4.

In summary, the size of graphene flakes can be controlled roughly by adjusting the inner diameter of the attached carbon tube. And for using rotating graphite plate and additional plasma torch, we can increase the injection rate of carbon source without thick graphene flakes and carbon impurities. So we expect that, large size of thin graphene flakes can be

fabricated through the optimization of experimental condition (inner diameter of carbon tube and rotating plate with additional plasma torch).

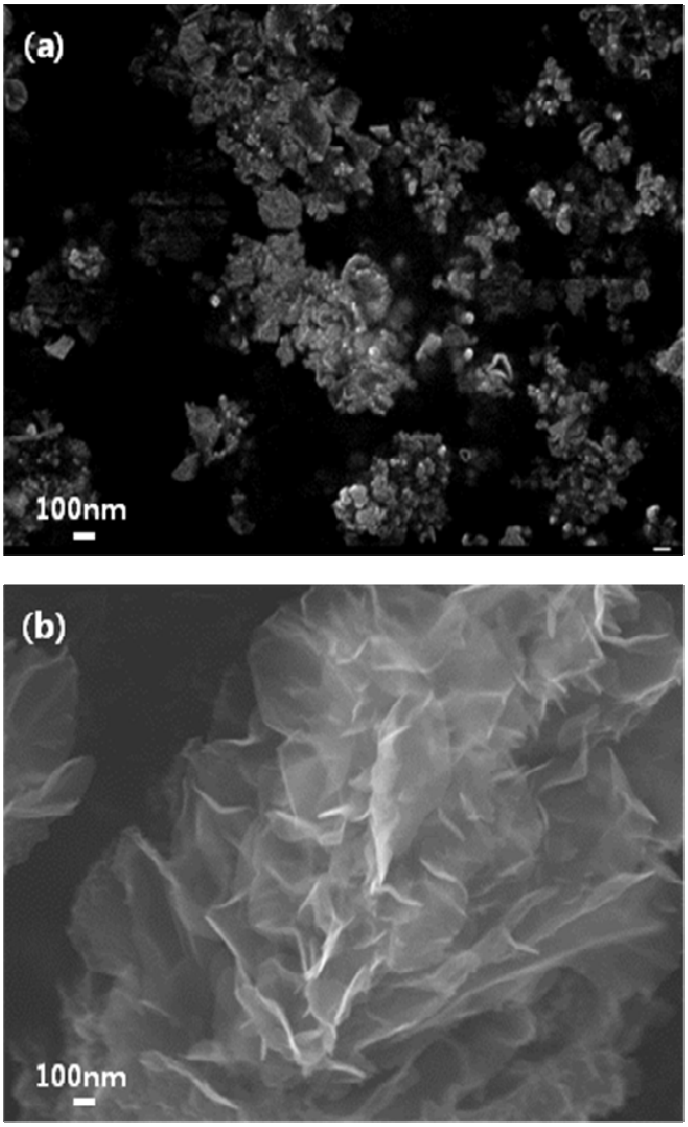


**Figure 5.3. (a) Methane gas (400 sccm) was inserted plasma system with fixed graphite plate and single plasma torch. (b) Methane gas (400 sccm) was inserted plasma system with rotating graphite plate and additional plasma torch.**

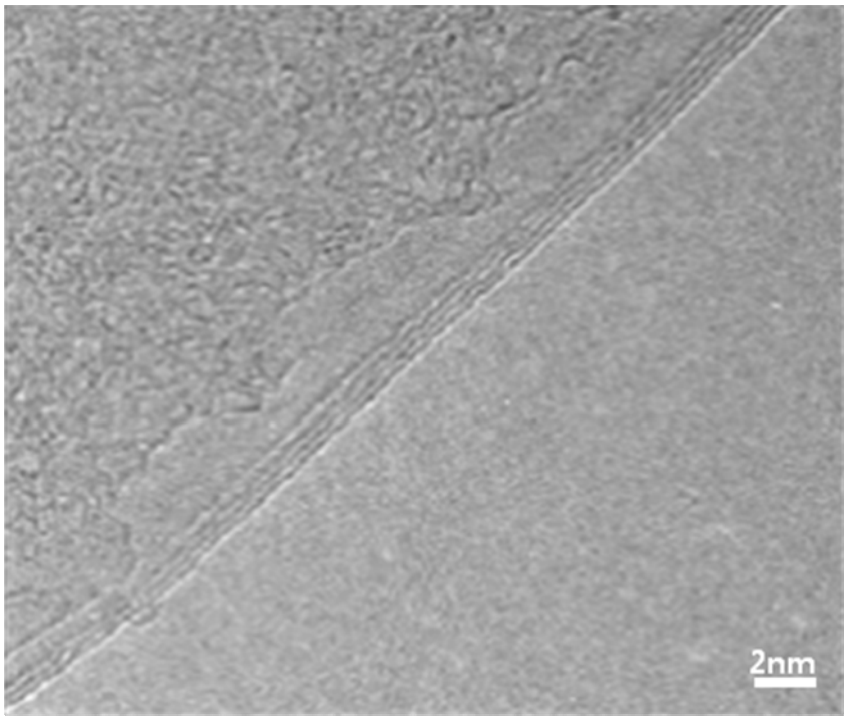


**Fig 5.4 TEM images of graphene flakes fabricated: methane gas (400 sccm) was inserted plasma system with rotating graphite plate and additional plasma torch.**

# CHAPTER 6. Size-controllable and low-cost fabrication of graphene quantum dots using thermal plasma jet system

We produced carbon soot by injecting ethylene gas continuously (at a rate of 2.5 L/min) into Ar plasma and attaching a carbon tube (5, 10, or 20 cm in length) to the anode. Figure 6.1 shows pictures of raw carbon soot produced by attaching a 20 cm carbon tube and its dispersing solutions.

**Figure 6. 1. Pictures of raw carbon soot and two dispersing solutions of carbon soot in ethanol. The carbon soot was produced by injecting ethylene continuously (2.5 L/min), with a carbon tube (20 cm in length) attached to the anode. The black solution was prepared by sonicating carbon soot in ethanol, while the pale yellow solution by stirring with a stirring rod.**

The production rate of carbon soot was 0.67 g/min (or 40 g/h). The black solution was prepared by sonicating carbon soot in ethanol, and the pale yellow solution by stirring with a stirring rod. This pale yellow solution emitted strong luminescence. Via sonication almost all of the carbon soot dispersed in ethanol, while by stirring with a stirring rod about 10% of the carbon soot was dispersed in ethanol. Both dispersing solutions were very stable for several months. Yellow solutions were obtained by dispersing carbon soot in toluene, pyridine, dimethyl sulfoxide (DMSO), and ethanol with a stirring rod. Among these, the toluene solution showed the brightest color. However, in water a very small portion of carbon soot was dispersed, even by sonication. Figure 6.2 shows the HRTEM images of onion-type materials and GQDs. In Figure 6.2 (a), onion-type carbon materials having contour-like fringes are observed. The TEM sample for onion-type materials was prepared by dispersing carbon soot, which was produced by attaching a 20 cm carbon tube, in ethanol by sonication. The dominant species of carbon soot were onion-type materials. Figure 6.2 (b) shows the high-resolution TEM (HRTEM) image of a GQD, which shows the high crystallinity of GQDs, with

lattice parameter 0.32 nm, and (002) lattice fringes of graphene. The corresponding fast Fourier transform (FFT) pattern is shown in the inset of Figure 6.2 (b). It shows a hexagonal pattern without any satellite spots. Single-layer graphene shows no satellite spots.[81] Therefore, we can conclude that our GQDs are single-layered.

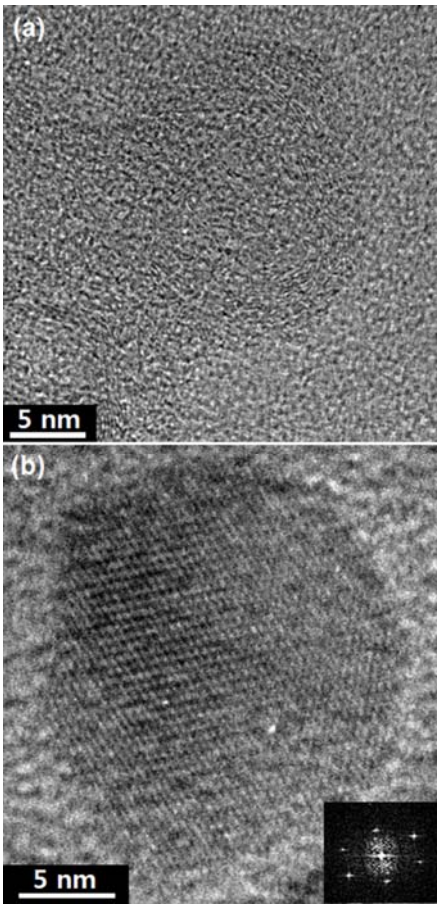


**Figure 6.2. HRTEM images of (top) onion-type carbon materials and (bottom) GQDs, insert is the 2D FFT pattern.**

This is supported by the atomic force microscopy (AFM) analysis of our GQDs (see Figure 6.3). The height profile of the line in Figure 6.3 shows that the thickness of the GQDs is less than 1 nm, which is in good agreement with the reported value for single-layered graphene.[87] The TEM and AFM samples for GQDs were prepared by dispersing carbon soot in ethanol by stirring with a stirring rod.

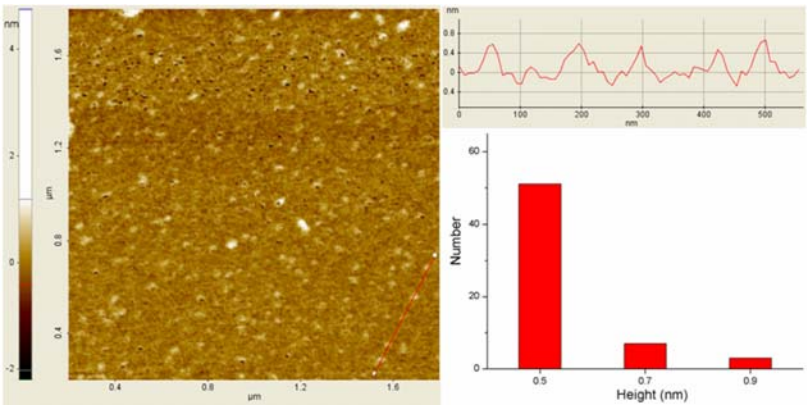


**Figure 6.3. AFM image and height distributions of 19 nm GQDs, and the height profile along the arrow. Some GQDs are clearly aggregated, and the height distributions were based on only the height of isolated GQDs**

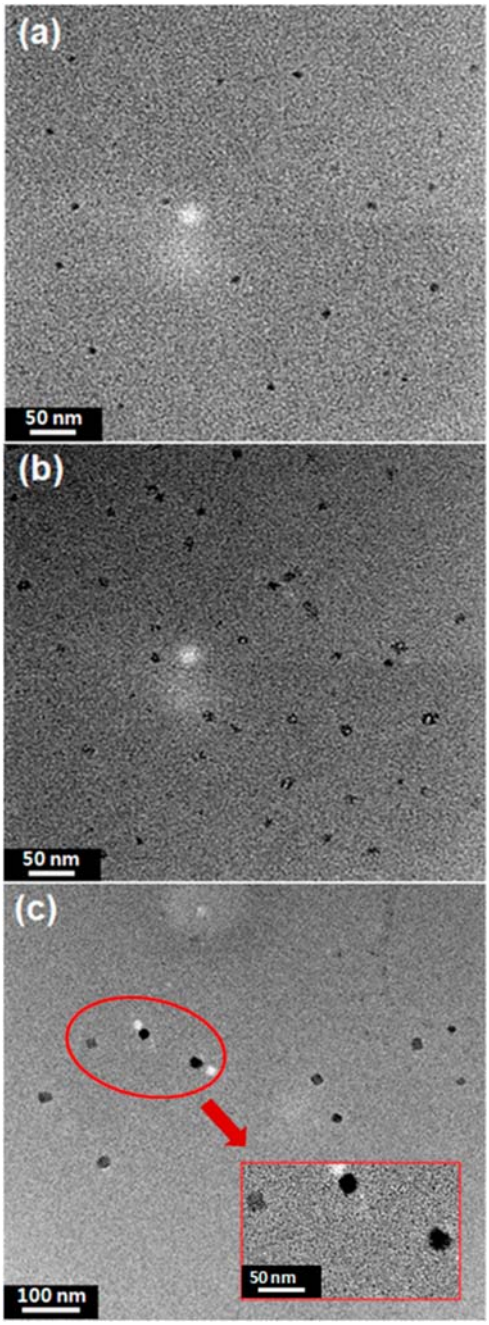


**Figure 6.4. TEM images of GQDs extracted from three kinds of carbon soot produced by attaching carbon tubes of three different lengths to the anode. The length of the carbon tube attached was (a) 5, (b) 10, and (c) 20 cm. The average size of GQDs was about (a) 10 nm, (b) 14 nm, and (c) 19 nm**.

Figure 6.4 shows the TEM images of GQDs extracted from three kinds of carbon soot produced by attaching a carbon tube (5, 10, or 20 cm in length) to the anode. These TEM samples were prepared by stirring three kinds of carbon soot in ethanol with a stirring rod. No onion-type carbon materials are observed. This means that, when carbon soot was dispersed in ethanol using a stirring rod, only GQDs were dispersed in the ethanol. It is a very simple and low-cost process. The weight percent of GQDs in carbon soot, based on the amount extracted in ethanol, was about 10%. According to the analysis of the TEM images, the size of the GQDs extracted from carbon soot produced by attaching a 5 cm carbon tube was in the range of 7 to 11 nm (see Figure 6.4(a)), while it was in the range of 11 to 15 nm for a 10 cm tube (see Figure 6.4(b)) and in the range 17 to 23 nm for a 20 cm tube (see Figure 6.4(c)). The size distributions are shown in Figure 6.5. The average sizes were about 10, 14, and 19 nm.

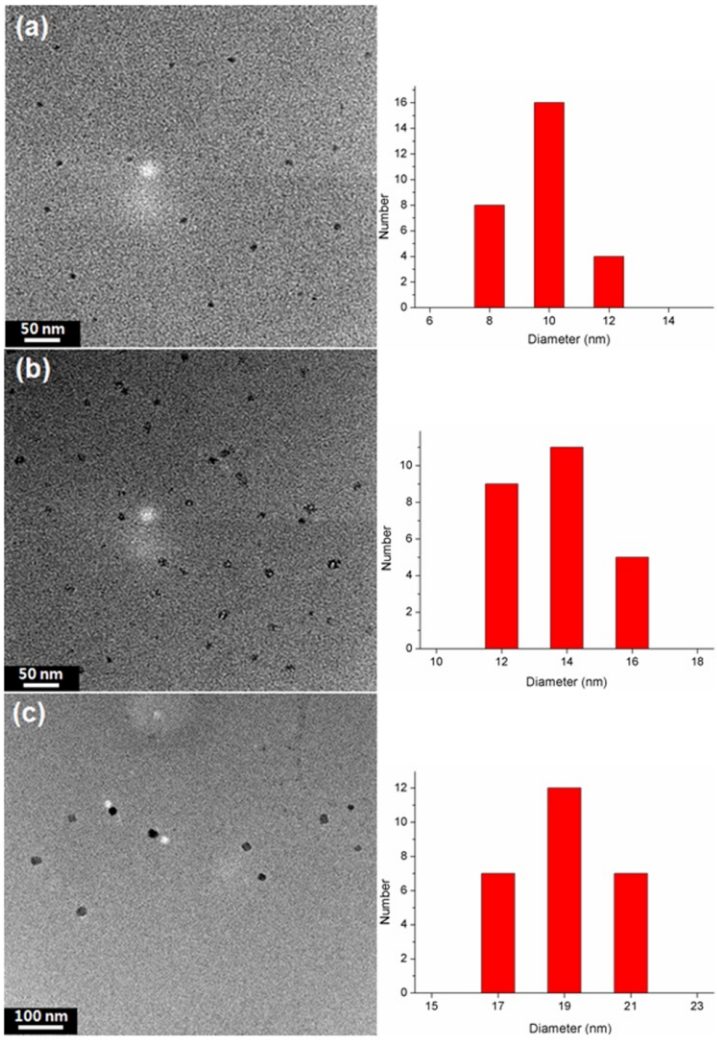


**Figure 6.5. TEM images and size distributions of GQDs extracted from three kinds of carbon soot produced by attaching carbon tube of three different lengths to the anode. The length of the carbon tube attached was (a) 5, (b) 10, and (c) 20 cm. The average size of GQDs was about (a) 9.7 nm, (b) 13.7 nm, and (c) 19 nm. The number of GQDs in the TEM images (a) and (c) were not enough, and the size distributions for (a) and (c) were included the data measured from other TEM images that are not shown here.**

The absolute quantum yields of these GQDs were 13.5%, 12.2%, and 9.6%, respectively (see Table 6.1). The average size of GQDs increased with increasing anode-attached carbon tube length. Under high ethylene injection rates, collisions between carbon atoms would take place mostly during flow through the carbon tube. Since the atomic beam was dispersed into a chamber after passing through the tube, collision reactions could take place only during flow through the carbon tube. Therefore, the reaction time would increase linearly when increasing the length of the tube. Increasing the reaction time would also increase the total number of collisions. Therefore, it is concluded that the average size of GQDs could be controlled by varying the length of the carbon tube attached to the anode.

| Average size of GQDs (nm) | $\lambda_{ex}$ (nm) | Absorbance of GQD solution at 402 nm | Quantum Yield(*Q.Y*) |
|---|---|---|---|
| 10 | 402 | 0.07 | 13.5 % |
| 14 | 402 | 0.07 | 12.2 % |
| 19 | 402 | 0.07 | 9.6 % |

**Table 6.1. Absolute quantum yield of GQDs (in absolute ethanol) measured using by absolute PL quantum yield measurement system QE-1200 (OTSUKA Electronics Co. LTD, Japan).**

UV-vis absorption, excitation-dependent photoluminescence (PL), and emission-dependent PL excitation (PLE) spectra of three GQD suspensions in ethanol are shown in Figures 6.6, Figure 6.7, and Figure 6.8.

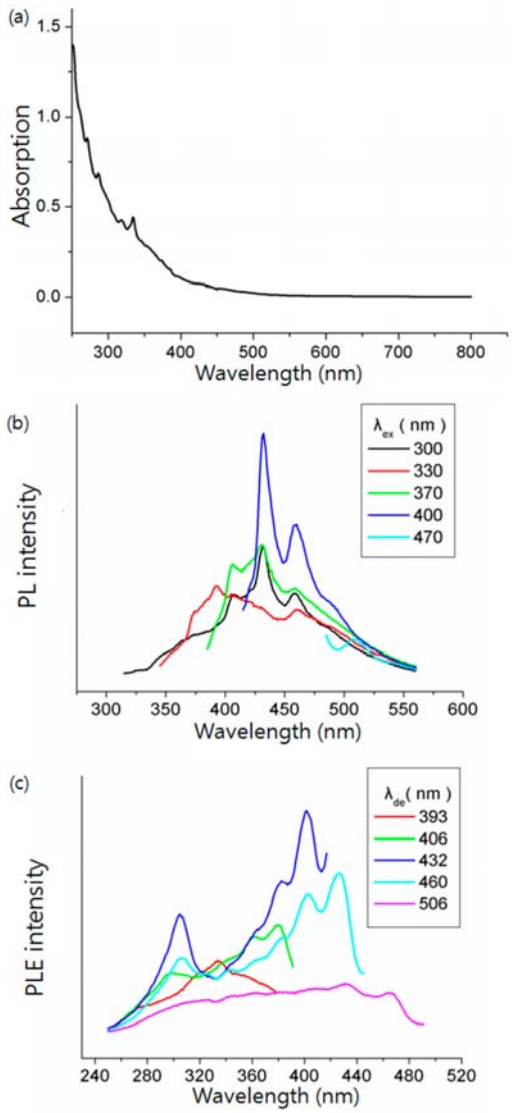


**Figure 6.6. (a) UV-vis absorption, (b) PL emission, and (c) PL excitation spectra of 19 nm GQD suspension in ethanol. The legends in (b) are the excitation wavelengths, and those in (c) are the detection wavelengths.**

The average sizes of GQDs in the three suspensions were 10, 14, and 19 nm. The GQD suspensions show a broad UV-vis absorption with shoulder-type peaks at 270, 280, 318, and 330 nm. Relative absorption intensity slightly increased when the average size of suspended GQDs increased (see Figure 6.7).

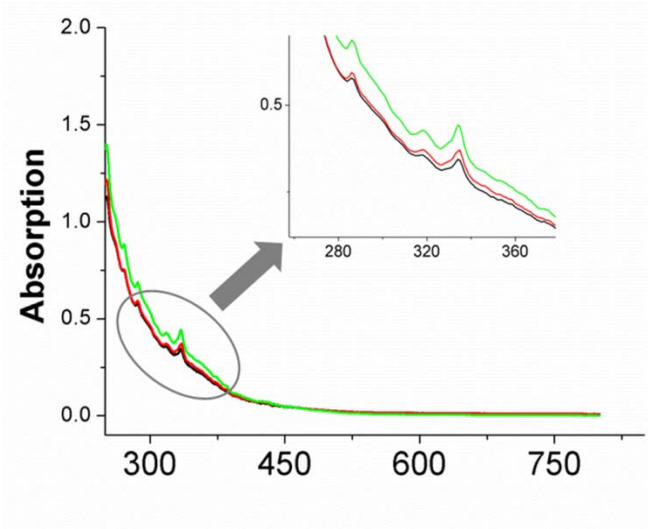


**Figure 6.7. UV-vis absorption spectra of three GQD suspensions in ethanol. The average sizes of GQDs in the three suspensions were 10, 14 and 19 nm.**

Three suspensions show almost the same excitation-dependent PL and emission-dependent PLE spectra except their relative intensity (see Figure 6.8). The same peak positions suggest that they share the same

luminescence origin. The PL peaks were observed near 375, 393, 406, 430, 460, 490, and 506 nm. The PL peak near 490 nm was very weak, and the peak centered at 506 nm was observed only by excitation with a relatively low energy light. The PLE spectra were measured by detecting at 393, 406, 432, 460, and 506 nm. For the PLE spectrum with the detection wavelength of 460 nm (2.70 eV), there are three strong absorption peaks at 426.4 (2.91 eV), 402.7 (3.08 eV), and 306.1 nm (4.05 eV) and three weak ones at near 380.7 (3.26 eV), 343.2 (3.61 eV), and 361.6 nm (3.43 eV). For the detection wavelength of 506 nm (2.45 eV), there are two weak peaks at 466.9 (2.66 eV) and 432.4 nm (2.87 eV).

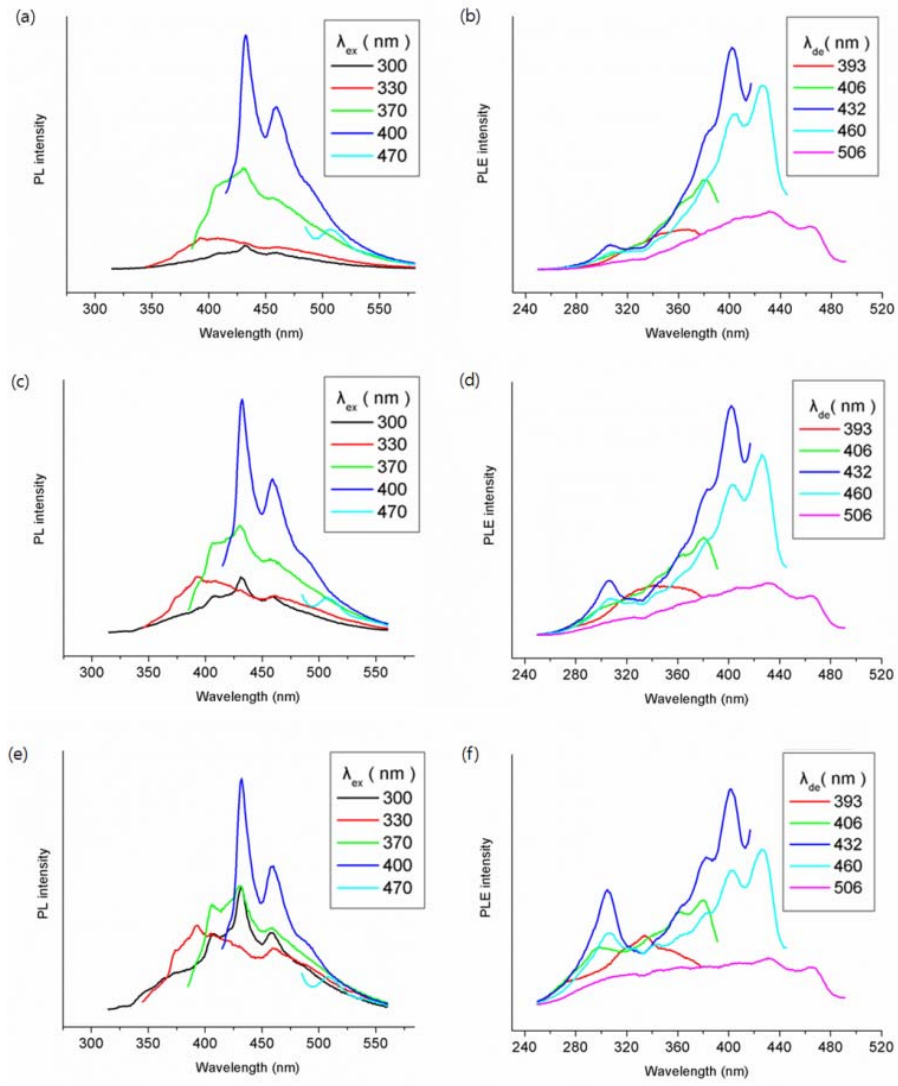


**Figure 6.8. Excitation-dependent photoluminescence (PL), and emission-dependent PL excitation (PLE) spectra of three GQD suspensions in ethanol. The average sizes of GQDs in the three suspensions were (a, b) 10, (c, d) 14 and (e, f) 19 nm.**

**Table 6.2. Absorption energies measured from the PLE spectra shown in Figure 6.6**

| $\lambda_{de.}$ \ ~$\lambda_{ab.}$ | 470 nm | 430 nm | 400 nm | 380 nm | 360 nm | 340 nm | 310 nm | 290 nm |
|---|---|---|---|---|---|---|---|---|
| 506 nm ( 2.45 eV ) | 467.8 nm ( 2.66 eV ) w | 432.4 nm (2.87 eV ) w | | | | | | |
| 460 nm ( 2.70 eV ) | | 426.4 nm ( 2.91 eV ) vs | 402.7 nm ( 3.08 eV ) s | 380.7 nm ( 3.26 eV ) w | 361.6 nm ( 3.43 eV ) w | 343.2 nm ( 3.61 eV ) w | 306.1 nm ( 4.05 eV ) s | |
| 432 nm ( 2.87 eV ) | | | 402.4 nm ( 3.08 eV ) vs | 381.4 nm ( 3.25 eV ) s | | | 305.5 nm ( 4.06 eV ) vs | |
| 406 nm ( 3.05 eV ) | | | | 379.5 nm ( 3.27 eV ) s | 361.5 nm ( 3.43 eV ) w | | | 293.8 nm ( 4.22 eV ) w |
| 393 nm ( 3.16 eV ) | | | | | | 334.0 nm ( 3.71 eV ) m | | |

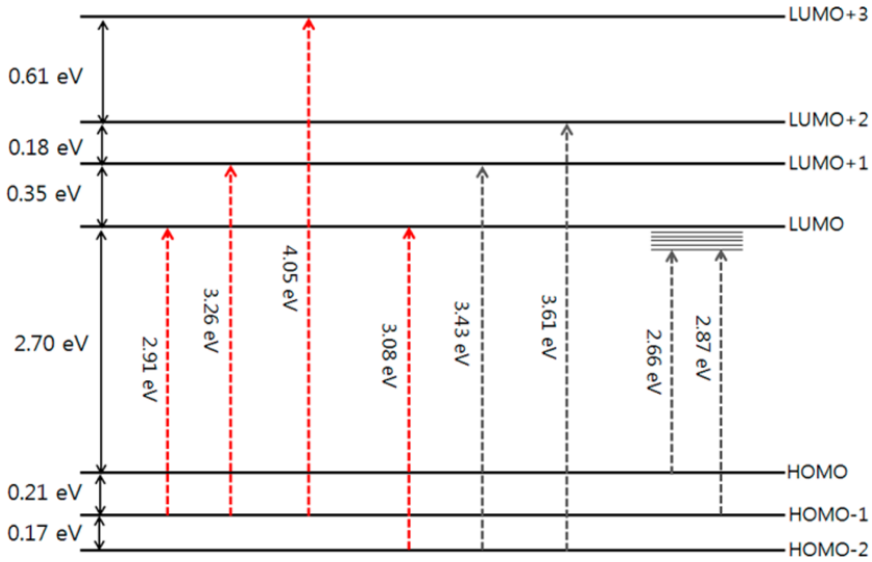


**Figure 6.9. Schematic of the electric structure of our GQDs based on the PLE data shown in Figure 5. The HOMO and LUMO+2 are singlet, and the others are triplet. The strong PLE transitions are shown in red.**

The absorption energies measured from the PLE spectra are summarized in Table 6.2, and a schematic of the electric structure is shown in Figure 6.9. The

electric structure consists of seven levels. The relative energy levels except the HOMO were determined simply by arranging the absorption energy data. Determination of the HOMO will be discussed below. It should be mentioned that the energy gaps shown in Figure 6.9 are based on the data of electronic transitions accompanied by vibrational transitions, and these values are not pure electronic transition energies.[90] The HOMO-HOMO-1 gap has been determined by assuming that the states reached by absorption of the lights of 2.66 eV from the HOMO and 2.87 eV from the HOMO-1 are the same state. The energy difference is 0.21 eV. Therefore, the HOMO lies 0.21 eV above the HOMO-1. Some observed energies, particularly for the energies of very weak absorptions, are slightly different from the energy gaps shown in the electronic structure, which was based on mainly the data measured from the strong absorption peaks. The weak absorptions are mainly due to spin-forbidden transitions, while the strong absorptions spin-allowed ones. Their transition mechanisms are different, and the vibrational levels involved in a spin-forbidden transition are different from those in a spin-allowed transition.[90] Therefore, when two transitions take place between any given

two electric states, the center position of a weak absorption peak could be slightly different from that of the strong one. Radovic and Bockrath proposed that for the oxygen-free edges of graphene sheets or quantum dots, free zigzag sites are carbene-like, with a triplet ground state being most common, whereas free armchair sites are carbyne-like, with a singlet ground state being most common.[89] The electronic structures of both types have seven energy levels, and two of them are singlet and the others are triplet.[91] In the PL spectrum with 400 nm excitation, there is a weak shoulder near 490nm(2.53 eV), whose energy is slightly lower than the HOMO-LUMO gap (2.7 eV). The weak luminescence is mainly due to the spin-forbidden transition. This means that HOMO and LUMO have a different multiplicity. For the PLE spectrum with the detection wavelength of 432 nm (2.87 eV), there are three strong absorption peaks at 402.4 (3.08 eV), 381.4 (3.25 eV), and 305.5 nm (4.06 eV). These energies correspond to the energy differences between HOMO2 and LUMO, HOMO-1 and LUMO+1, and HOMO-1 and LUMO+3, respectively. Since strong peaks are mainly due to spin-allowed transitions, the HOMO-1, HOMO-2, LUMO, LUMO+1, and LUMO+3 have the same multiplicity. The

energy difference between HOMO-2 and LUMO+2 levels is 3.61 eV, which is well distinguished from other energy values. The absorption peak at 343 nm(3.61 eV) is very weak in all the PLE spectra except the one with the detection wavelength of 393 nm(3.16 eV). The relatively strong PL peak centered at 393 nm (3.16 eV) may correspond to the luminescence from LUMO+2 to HOMO, whose gap is 3.23 eV. A strong luminescence could take place when the HOMO and LUMO+2 have the same multiplicity. By the calculation of Radovic and Bockrath, among seven levels two of them are singlet and the others are triplet.[91] Therefore, it is concluded that HOMO and LUMO+2 are singlet and the others are triplet. Since the HOMO is singlet, our GQDs may have carbyne-like edges.[91] The H-free armchair sites of GQDs become carbyne-like edges when triple bonds are made by rehybridizing. Therefore, we propose that the PL peaks observed can be attributed to electronic transitions between energy levels of the GQDs having carbyne-like edges. Our GQDs dispersed in organic solvents such as toluene, but did not disperse in water. Carbyne is o-benzyne, which is a nonpolar compound and does not dissolve in water. The dispersion properties of our GQDs also

support that they have carbynelike edges. The PL and PLE spectra of three suspensions whose average GQD sizes were 10, 14, and 19 nm were almost the same except for their relative intensity (see Figures 6.8). With a decrease in the average size of GQDs, the relative intensity of the PLE peaks near 300 nm was decreased. Also, the relative intensity of PL spectra excited by 300 and 330 nm light was decreased. These behaviors seem to be due to a quantum size effect. However, further studies are needed to gain a better understanding of the cause of these behaviors. It is known that the PL characteristic of GQDs is critically affected by the content of oxygen.[83] In principle, oxygen is not contained in our fabrication, since only Ar and ethylene gases have been added into a plasma system as the plasma gas and carbon source, respectively. According to the energy-dispersive X-ray spectroscopy (EDS) analysis of carbon soot including GQDs, no oxygen was observed from carbon soot not exposed to air, while oxygen (3.60 atomic %) was observed from carbon soot exposed to air for about 30 min (see Figure 6.10).

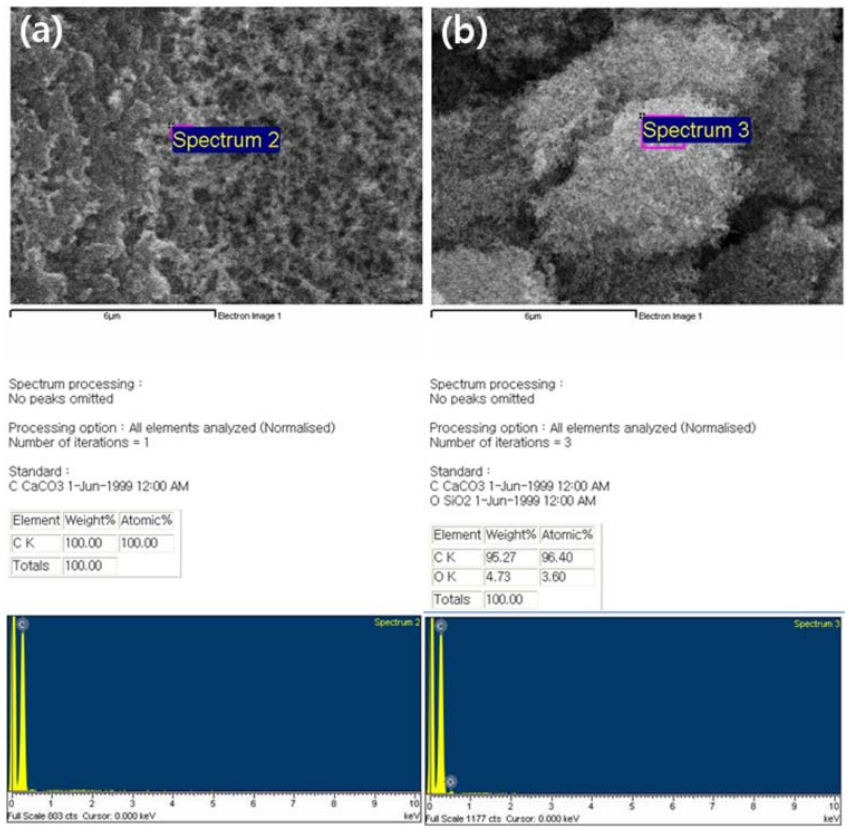


**Figure 6.10. SEM images and EDS spectra of carbon soot: measured from (a) freshly fabricated carbon soot, not exposed to air and (b) carbon soot exposed to air for about 3o min. The content of oxygen is zero in (a) and 3.60 atomic% in (b).**

X-ray photoelectron spectroscopy (XPS) was performed to determine the composition of our GQDs (see Figure 6.11). The measured spectra could be deconvoluted into four surface components, corresponding to sp2 (C=C) at binding energy of 284.5 eV, sp3 (C-C and C-H) at 285.5 eV, C-OH at 286.6 eV, and O=C-OH at 288.6 eV.

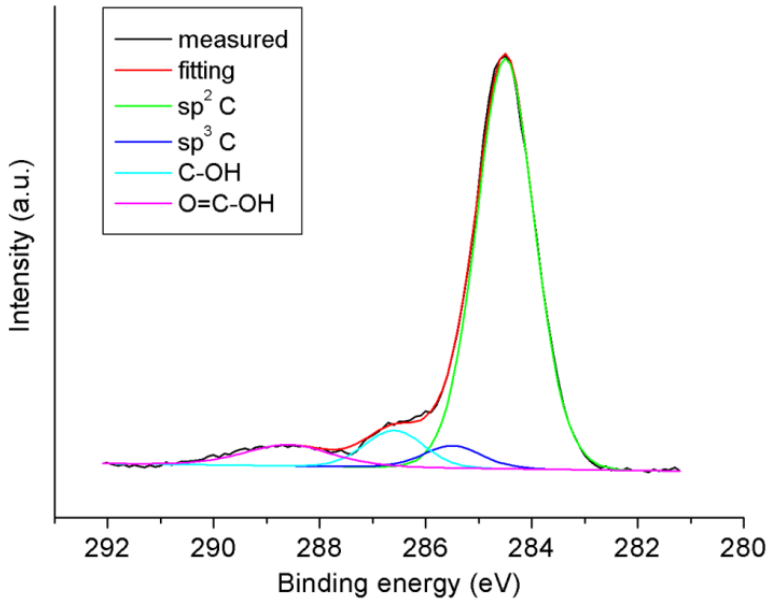


**Figure 6.11. XPS C1s spectrum of GQDs whose average size was 19 nm. The spectrum can be deconvoluted into four surface components, corresponding to sp2 (C=C) at binding energy of 284.5 eV, sp3 (C-C, and C-H) at 285.5 eV, C-OH at 286.6 eV, as well as O=C-OH at 288.6 eV. The molar ratios of these species are 81.8, 4.4, 7.4, and 6.4%, respectively. Oxygen might be included during the specimen preparation process, since the fresh carbon soot did not contain oxygen.**

The bands corresponding to C-OH and O=C-OH were relatively weak. Oxygen might be included during the specimen preparation process, since the fresh carbon soot did not contain oxygen. This fabrication method of GQDs is basically different from our previous fabrication method[75] of graphene. In our previous method, graphene is made on the surface of the graphite plate by an epitaxial growth when the carbon atoms of a carbon atomic beam collide with

the graphite plate placed in the path of the carbon atomic beam. However, GQDs are made by a gas phase collision reaction, since no graphite plate is placed in the path of the carbon atomic beam. The injection rate of ethylene was 2.5 L/min, which is relatively very high. In the previous method, the injection rate of ethanol was 0.1 mL/min, which corresponds to 40 mL/min in the gas phase.[77] For one's information, the injection rate of Ar plasma gas was 13.5 L/min. By a simple calculation, the proportion of carbon atoms in the atomic beam is roughly 17.5%, since two carbon and four hydrogen atoms are generated when an ethylene molecule is atomized. Therefore, under our experimental conditions, the collisions between carbon atoms might take place heavily during flow through the attached carbon tube. Our method is a relatively low-cost process. Our thermal plasma system including a dc power supply is a relatively inexpensive setup, and ethylene is a cheap chemical. Also, the total electrical consumption is not substantial. Our fabrication is a continuous process. The production rate of carbon soot was 0.67 g/min (or 40 g/h) for a 2.5 L/min injection rate of ethylene gas, and the weight percent of GQDs in carbon soot, based on the amount extracted in ethanol, was about

10%. By simple calculation, a plasma system could produce 40 g of GQDs per day by assuming 10 h operation. This means that mass production of GQDs could be possible if we operated many plasma systems. In the fabrication of our GQDs, no chemical treatment was involved except for dispersion in ethanol, which is a mild solvent. Also, the fabrication temperature was relatively high, and it is known that the crystallinity of carbon materials such as carbon nanotubes increases with increasing fabrication temperature.[81,82] Therefore, our GQDs ought to have a good crystallinity. A Raman spectrum of our GQDs is shown in Figure 6.12. The G band near 1596 $cm^{-1}$ was stronger than the D band near 1353 $cm^{-1}$. The D band is known due to the presence of structural disorder in the graphene sheets. A higher G/D intensity ratio indicates better crystallinity of the GQDs. However, the edges are always seen as defects, and the portion of edges increases with decreasing GQD size. Generally, GQDs show a relatively low G/D intensity ratio.[58,69,92,85] The intensity ratio of our GQDs was relatively high, 1.6.

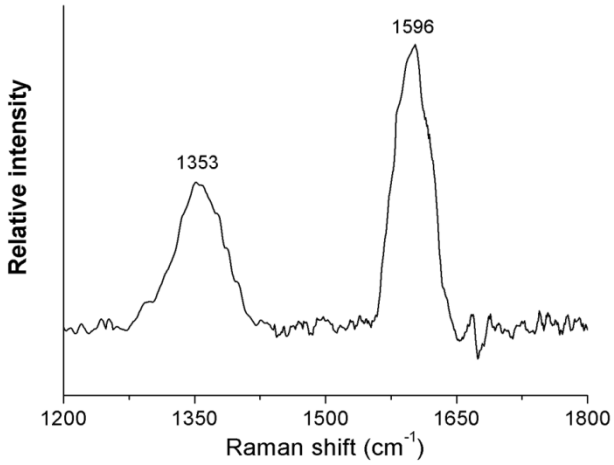


**Figure 6.12. Raman spectrum of GQDs, whose average size was 19 nm, measured by excitation with 514.5 nm Ar ion laser line. The G peak near 1596 $cm^{-1}$ is stronger than the D peak near 1353 $cm^{-1}$. The G/D intensity ratio is about 1.6.**

In summary, We have developed a size-controllable and low-cost GQD fabrication method using thermal plasma jet. A large amount of ethylene gas was injected continuously into Ar plasma to generate a carbon atomic beam. The beam was then flowed through a carbon tube attached to the anode, and then dispersed into a chamber. Carbon materials including GQDs were made by a gas phase collision reaction. The production rate of carbon soot was 40 g/hour for a 2.5 L/min injection rate of ethylene. We could extract isolated GQDs from carbon soot simply by dispersing it in ethanol using a stirring rod.

The weight percent of GQDs in carbon soot, based on the amount extracted in ethanol, was about 10%. We could control the average size of GQDs, with a relatively narrow size distribution, by varying the length of the carbon tube attached. Our method is a size-controllable, low-cost and mass producible process. The electric structure based on the PL and PLE data has a singlet ground state, and it is in good agreement with that of carbyne. Our GQDs were dispersed in organic solvents like toluene, whereas not dispersed in water. These properties also support that our GQDs have carbyne-like edges. The PL peaks observed are attributed to electronic transitions between energy levels of the GQDs having carbyne-like edges.

**REFERENCES**


1. Geim, A. K. and Novoselov, K. S., Nature Mater. **6**, 183 (2007).

2. PardiniI, L. C.; NetoII, F. L.; Almeida Fereira, J. L., Materials Research **9**, (2006).

3. Novoselov, K. S.; Geim, A. K.; Morozov, S. V.; Jiang, D.; Zhang, Y.; Dubonos, S. V.; Grigorieva, I. V. and Firsov, A. A., Science **306**, 666 (2004).

4. Mark, W., Physics Today, 21 (2006).

5. Novoselov, K. S.; Jiang, D. ; Schedin, F.; Booth, T. J.; Khotkevich, V. V.; Morozov, S. V. and Geim, A. K., Proc. Natl Acad. Sci. USA **102**, 10451 (2005).

6. Novoselov, K. S.; Geim, A. K.; Morozov, S. V.; Jiang, D.; Katsnelson, M. I.; Grigorieva, I. V.; Dubonos, S. V. and Firsov, A.A., Nature **438**, 197 (2005).

7. Zhang, Y.; Tan, J. W.; Stormer, H. L. and Kim, P., Nature **438**, 201 (2005).

8. Chen, J. H.; Jang, C.; Xiao, S.; Ishigami, M., and Fuhrer, M. S., Nature Nanotechnology **3,** 206 (2008).

9. Akturk, A. and Goldsman, N., Journal of Applied Physics **103**, 053702 (2008).

10. Service, R. F., Science **324**, 875 (2009)

11. Lee, C.; Wei, X.; Kysar, J. W. and Hone, J., Science **321**, 385 (2008).

12. Balandin, A. A.; Ghosh, S.; Bao, W. Z.; Calizo, I.; Teweldebrhan, D.;

Miao, F. and Lau, C. N., Nano Lett. **8**, 902 (2008).

13. Kuzmenko, A. B.; Van Heumen, E.; Carbone, F. and Van Der Marel, D., Physical Review Lett. **100** (11), 117401 (2008).

14. Sutter, P., Nature Mater. **8** (3), 171 (2009).

15. Berger, C.; Song, Z.; Li, X.; Wu, X.; Brown, N.; Naud, C.; Mayou, D.; Li, T.; Hass, J.; Marchenkov, A. N.; Conrad, E. H.; First, P. N. and de Heer, W. A., Science, **312**, 1191 (2006).

16. Hass, J.; Feng, R.; Li, T.; Li, X.; Zong, Z.; de Heer, W. A.; First, P. N.; Conrad, E. H. C.; Jeffrey A. and Berger. C., Appl. Phys. Lett. **89**, 143106 (2006).

17. Kim, K. S.; Houk Jang, Y. Z.; Lee, S. Y.; Kim, J. M.; Kim, K. S.; Ahn, J. H.; Kim, P.; Choi J. Y. and Hong, B. H., Nature **457** (7230), 706 (2009).

18. Bae, S.; Kim, H.; Lee, Y.; Xu, X.; Park, J. S.; Zheng, Y.; Balakrishnan, J.; Lei, T.; Kim, H. R.; Song, Y. I.; Kim, Y. J.; Kim, K. S.; Özyilmaz, B.; Ahn, J. H.; Hong, B. H. and Iijima, S., Nature Nanotechnology **5** (8), 574 (2010).

19. Li, X.; Cai, W.; An, J.; Kim, S.; Nah, J.; Yang, D.; Piner, R.; Velamakanni, A.; Jung, I.; Tutuc, E.; Banerjee, S. K.; Colombo, L. and Ruoff R. S., Science **324** (5932), 1312 (2009).

20. Hummers, W. and Offeman, R., J. Am. Chem. Soc. **80**, 1339 (1958).

21. Li, D.; Muller, M. B.; Gilje, S.; Kaner, R. B. and Wallace, G. G. Nature Nanotechnology **3**, 101 (2008).

22. Li, D. and Kaner, R.B., Science **320**, 1170 (2008).

23. Dresselhaus, M .S. and. Dresselhaus, G., Adv. Phys **51**, 186 (2002).

24. Li, X. L.; Zhang, G. Y.; Bai, X. D.; Sun, X. M.; Wang, X. R.; Wang, E. and Dai, H. J., Nature Nanotechnology **3** (9), 538 (2008).

25. Hernandez, Y.; Nicolosi, V.; Lotya, M.; Blighe, F. M.; Sun, Z. Y.; De, S.; McGovern, I. T.; Holland, B.; Byrne, M.; Gun'ko, Y. K.; Boland, J. J.; Niraj, P.; Duesberg, G.; Krishnamurthy, S.; Goodhue, R.; Hutchison, J.; Scardaci, V.; Ferrari, A. C. and Coleman, J. N., Nature Nanotechnology **3**(9), 563 (2008).

26. Lotya, M.; Hernandez, Y.; King, P. J.; Smith, R. J.; Nicolosi, V.; Karlsson, L. S.; Blighe, F. M.; De, S.; Wang, Z. M.; McGovern, I. T.; Duesberg, G. S.; Coleman, J. N., J. Am. Chem. Soc. **131**(10), 3611 (2009).

27. Tung, V. C.; Allen, M. J.; Yang, Y.; Kaner, R. B., Nature Nanotechnology **4** (1), 25 (2009).

28. Wang, X.; Zhi, K. and Müllen, K., Nano Lett. **8** (1), 323 (2007).

29. Eda, G.; Fanchini, G. and Chhowalla, M., Nature Nanotechnology **3** (5), 270 (2008).

30. Lemme, M. C.; Echtermeyer, T. J.; Baus, M. and Kurz H., IEEE Electron Device Lett. **28** (4), 282 (2007).

31. Lin, Y. M.; Dimitrakopoulos, C.; Jenkins, K. A.; Farmer, D.B.; Chiu, H. Y.; Grill, A. and Avouris, P., Science **327** (5966), 662 (2010).

32. Schedin, F.; Geim, A. K.; Morozov, S. V.; Hill, E. W.; Blake, P.; Katsnelson, M. I. and Novoselov, K. S., Nature Mater. **6** (9), 652 (2007).

33. Mukhopadhyay, P. and Gupta, R. K., CRC Press Taylor & Francis Group, 202 (2013).

34. Kirkland, N. T.; Schiller, T.; Medhekar, N. and Birbilis N., Science **56** 1 (2012).

35. Stoller, M. D.; Park, S.; Zhu, Y.; An, J. and Ruoff, R. S., Nano Lett. **8**, 3498 (2008).

36. David, L.; Bhandavat, R.; Kulkarni, G.; Pahwa, S.; Zhong, Z. and Singh, G., Applied Materials & Interface **5** (3), 546 (2013).

37. Radhakrishnanz, G.; Cardema, J. D.; Paul M. Adams, P. M.; Kim, H. I. and Foran, B., J. Electrochemical Soc. **159**, 752 (2012).

38. Yao, F.; Güneş, F.; Ta, H. Q.; Lee, S. N.; Chae, S. J.; Sheem, K. Y.; Cojocaru, C. S.; Xie, S. S. and Lee Y. H., J. Am. Chem. Soc. **134** (20), 8646 (2012).

39. Baker, S. N. and Baker, G. A., Angew. Chem. Int. Ed. **49**, 6726 (2010).

40. Hu, S. L.; Niu, K. Y.; Sun, J.; Yang, J.; Zhao, N. Q. and Du, X. W. J. Mater. Chem. **19**, 484 (2009).

41. Sun, Y. P.; Wang, X.; Lu, F. S.; Cao, L.; Meziani, M. J.; Luo, P. J. G.; Gu, L. R. and Veca, L. M., J. Phys. Chem. C **112**, 18295 (2008).

42. Zhou, J. G.; Booker, C.; Li, R. Y.; Zhou, X. T.; Sham, T. K.; Sun, X. L. and Ding, Z. F., J. Am. Chem. Soc. **129**, 744 (2007).

43. Liu, R. L.; Wu, D. Q.; Liu, S. H.; Koynov, K.; Knoll, W. and Li, Q., Angew. Chem., Int. Ed. **48**, 4598 (2009).

44. Zhou, J. G.; Booker, C.; Li, R. Y.; Sun, X. L.; Sham, T. K. and Ding, Z. F., Chem. Phys. Lett. **493**, 296 (2010).

45. Pan, D. Y.; Zhang, J. C.; Li, Z.; Wu, C.; Yan, X. M. and Wu, M. H., Chem. Commun. **46,** 3681 (2010).

46. Bourlinos, A. B.; Stassinopoulos, A.; Anglos, D.; Zboril, R.; Georgakilas, V. and Giannelis, E. P., Chem. Mater. 20, 4539 (2008).

47. Liu, H. P.; Ye, T. and Mao, C., Angew. Chem., Int. Ed., **46**, 6473 (2007).

48. Tian, L.; Ghosh, D.; Chen, W.; Pradhan, S.; Chang, X. J. and Chen, S. W., Chem. Mater. **21**, 2803 (2009).

49. Yu, S. J.; Kang, M. W.; Chang, H. C.; Chen, K. M. and Yu, Y. C., J. Am. Chem. Soc. **127**, 17604 (2005).

50. Zhu, H.; Wang, X. L.; Li, Y. L.; Wang, Z. J.; Wang, F. and Yang, X. R. Chem. Commun. 5118 (2009).

51. Bottini, M.; Balasubramanian, C.; Dawson, M. I.; Bergamaschi, A.; Bellucci, S. and Mustelin, T., J. Phys. Chem. B **110**, 831 (2006).

52. Wang, X.; Cao, L.; Lu, F. S.; Meziani, M. J.; Li, H.; Qi, G.; Zhou, B.; Harruff, B. A.; Kermarrec, F. and Sun, Y. P., Chem. Commun. 3774 (2009).

53. Tian, L.; Song, Y.; Chang X. J. and Chen, S. W., Scr. Mater. **62**, 883 (2010).

54. Zong, J.; Zhu, Y. H.; Yang,; Shen, J. H. and Li, C. Z., Chem. Commun. **47,** 764 (2011).

55. Ponomarenko, L. A.; Schedin, F.; Katsnelson, M. I.; Yang, R.; Hill, E. W.;

Novoselov, K. S. and Geim, A. K., Science **320**, 356 (2008).

56. Gupta, V.; Chaudhary, N.; Srivastava, R.; Sharma, G, D.; Bhardwaj, R. and Chand, S., J. Am. Chem. Soc. **133**, 9960 (2011).

57. Shen, J.; Zhu, Y.; Yang, X.; Zong, J.; Zhang, J. and Li, C., New J. Chem. **36**, 97 (2012).

58. Pan, D. Y.; Zhang, J. C.; Li, Z. and Wu, M. H., Adv. Mater. **22**, 734 (2010).

59. Shen, J.; Zhu, Y.; Chen, C.; Yang, X. and Li, C., Chem. Commun. **47**, 2580 (2011).

60. Eda, G.; Lin, Y. Y.; Mattevi, C.; Yamaguchi, H.; Chen, H. A.; Chen, I. S.; Chen, C. W. and Chhowalla, M., Adv. Mater. **22**, 505 (2010).

61. Gokus, T.; Nalr, R. R.; Bonettl, A.; Bohmler, M.; Lombardo, A.; Novoselov, K. S.; Gelm, A. K.; Ferrarl, A. C. and Hartschuh, A., ACS Nano **3,** 3963 (2009).

62. Yan, X.; Cui, X. and Li, L.S., J. Am. Chem. Soc., **132**, 5944 (2010).

63. Hamilton, I. P.; Li, B.; Yan, X. and Li, L. S., Nano Lett. **11**, 1524 (2011).

64. Li, L. S. and Yan, X., J. Phys. Chem. Lett. **1**, 2572 (2010).

65. Mueller, M. L.; Yan, X.; McGuire, J. A. and Li, L. S., Nano Lett. **10**, 2679 (2010).

66. Yan, X.; Cui, X.; Li, B. S. and Li, L. S., Nano Lett. **10**, 1869 (2010).

67. Mueller, M. L.; Yan, X.; Dragnea, B. and Li, L. S., Nano Lett. **11**, 56 (2011).

68. Ritter, K. A. and Lyding, J. W., Nature Mater. **8**, 235 (2009)..

69. Peng, J.; Gao, W.; Gupta, B. K.; Liu, Z.; Romero-Aburto, R.; Ge, L.; Song, L.; Alemany, L. B.; Zhan, X.; Gao, G.; Zhu, J. J. and Ajayan, P, M., Nano Lett. **12**, 844 (2012).

70. Zhu, S. J.; Zhang, J. H.; Qiao, C. Y.; Tang, S. J.; Li, Y. F.; Yuan,W. J.; Li, B.; Tian, L.; Liu, F.; Hu, R.; Zhang, J.; Sun, H. and Yang, B., Chem. Commun. **47**, 6858 (2011).

71. Cheng, H.; Zhao, Y.; Fan, Y.; Xie, X.; Qu, L.; Shi, G., ACS Nano **6**, 2237 (2012).

72. Shen, J.; Zhu, Y.; Yang, X. and Li, C., Chem. Commun. **48**, 3686 (2102).

73. Chen, J. L. and. Yan, X. P., Chem. Commun. **47**, 3135 (2011).

74. Lee, J.; Kim, K.; Park, W, I.; Kim, B, H.; Park, J, H.; Kim, T, H.; Bong, S.; Kim, C, H.; Chae, G.; Jun, M.; Jung, Y. S. and Jeon, S., Nano Lett. **12**, 6078 (2012).

75. Yan, X.; Cui, X. and Li, L. S., J. Am. Chem. Soc. **132,** 5944 (2010).

76. Liu, R.; Wu, D.; Feng, X. and Müllen, K., J. Am. Chem. Soc. **133**, 15221 (2011).

77. Kim, J.; Heo, S. B.; Gu, G. H.; Suh, J. S., Nanotechnology **21**, 095601 (2010).

78.Ferrari, A. C.; Meyer, J. C.; Scardaci, V.; Casiraghi, C.; Lazzeri, M.; Mauri, F.; Piscanec, S.; Jiang, D.; Novoselov, K. S.; Roth, S. and Geim, A. K., Physical Review Lett. **97** (18), (2006).

79. Kudin, K. N.; Ozbas, B.; Schniepp, H. C.; Prud'homme, R. K.; Aksay, I. A.

and Car, R., Nano Lett. **8** (1), 36 (2008).

80. Dresselhaus, M. S. and Eklund, P. C., Science of Fullerenes and Carbon Nanotubes. Academic Press (1996).

81. Hahn, J.; Han, J. H.; Yoo, J. E.; Jung, H. Y. and Suh, J. S., Carbon 42 (4), 877 (2004).

82. Hahn, J.; Heo, S. B. and Suh, J. S., Carbon **43** (12), 2638 (2005).

83. Ci, L.; Song, L.; Jin, C.; Jariwala, D.; Wu, D.; Li, Y.; Srivastava, A.; Wang, Z. F.; Storr, K.; Balicas, L.; Liu, F. and Ajayan, P. M., Nature Mater. **9**, 430 (2010).

84. Zhu, S.; Zhang, J.; Tang, S; Qiao, C.; Wang, L.; Wang, H.; Liu, X.; Li, B.; Li, Y.; Yu, W.; Sun, H. and Yang, B., Adv. Func. Mater. **22**, 4732 (2012).

85. Liu, F.; Jang, M. H., Ha, H. D.; Kim, J. H.; Cho, Y. H. and Seo, T. S., Adv. Mater. **25**, 3657 (2013)

86. Shim, J,; Yun, J. M.; Yun, T.; Kim, P.; Lee, K. E.; Lee, W. J.; Ryoo, R.; Pine, D. J.; Yi, G. R.; Kim, S. O., Nano Lett. **14 (3)**, 1388 (2014).

87. Li, Z. Y.; Akhtar, S. M.; Kuk, J. H.; Kong, B. S. and Yang, O B. Materials Lett. **86**, 96 (2012).

88. Shih, P. T.; Dong, R. X.; Shen, S. Y.; Vittal, R.; Lin, J. J. and Ho, K. C., J. Mater. Chem. A **2**, 8742 (2014).

89. Gupta, A.; Chen, G.; Joshi, P.; Tadigadapa, S.; Eklund, P. C., Nano Lett. **6**, 2667 (2006).

90. Hollas, J. M., Ed. Modern Spectroscopy, John Wiley & Sons, Ltd, 2004.

91. Radovic, L. R.; Bockrath, B., J. Am. Chem. Soc. **127**, 5917 (2005).

92. Li, Y.; Hu, Y.; Zhao, Y.; Shi, G. Q.; Deng, L.; Hou, Y. B.; Qu, L. T., Adv. Mater. **23**, 776 (2011).

## 국문초록

그래핀은 탄소원자들이 $sp^2$ 결합을 하면서 벌집 격자 구조를 가지는 원자 두께의 2차원 물질이다. 2004년 영국 맨체스터 연구진들에 의해 발견된 그래핀은 현재까지도 많은 관심을 받으면서 연구가 활발하게 진행되고 있는데 그 이유는 그래핀이 가진 우수한 성질과 그래핀의 응용분야가 다양하기 때문이다. 먼저 그래핀은 전기적 성질이 매우 우수하다고 알려져 있다. 그래핀에서의 전하 이동속도는 현재 반도체 물질로 주로 사용되는 단 결정 실리콘 보다 100배는 빠르며 구리 보다 10배나 더 많은 전류를 흐를 수 있는 성질이 있다. 또한, 그래핀은 원자 두께의 매우 얇은 물질임에도 불구하고 강도가 우수하고 유연한 장점이 있으며 열전도성도 매우 우수하다고 알려져 있다. 이 밖에도 금속의 부식을 방지하는 성질, 전자파를 차폐하는 성질 등 우수하면서 흥미로운 성질을 지닌 물질이다. 이러한 성질로 인해 나노 복합소재, 전기전자 분야, 수소저장, 배터리, 센서 등 다양한 분야로의 응용이 기대되고 있다. 그래핀을 제조하는 방법은 매우 다양하며 현재까지도 계속 개발되고 있는데 그 중 가장 대표적인 방법으로 기계적 박리, 화학 기상증착, 산화-환원법 등이 있다. 먼저 기계적 박리법은 처음 그래핀을 개발 한 방법으로써 고정렬 열분해 흑연(HOPG)에서 스카치 테이프를 이용하여 그래핀 층을 벗겨내는 방식이다. 이 방법은 경우 간단한 방법으로 그래핀을 제조할 수 있다는 장점이 있지만 대면적의 그래핀을 제조하는 것은 불

가능한 단점이 존재한다. 화학 기상증착법은 탄화수소 가스를 전이 금속(주로 구리, 니켈이 사용) 기판 표면에 노출시켜 고온에서 포화하는 방법으로 이 때 기판의 온도를 낮추면 전이금속의 탄소 용해도가 감소하여 얇은 그래핀층이 생성되는 원리이다. 마지막으로 산화-환원법은 액체 기반의 방법으로 흑연을 산화 시키고 산화흑연을 다시 환원시키는 과정을 통해 그래핀을 제조하는 방법이다. 산화-환원법은 대량 생산과 분산된 그래핀 용액을 얻을 수 있는 장점이 있지만 산화-환원 과정을 거치면서 그래핀 고유의 우수한 성질이 감소되는 단점이 존재한다. 본 연구에서는 기존의 방법과 다른 새로운 방법을 통해 그래핀을 제조하여 기존의 방법들이 가지고 있던 단점들을 극복하고자 하였다. 바로 열플라즈마 장치를 이용하여 그래핀을 제조하는 방법인데 열플라즈마 장치를 간단히 설명하면 다음과 같다. 열플라즈마 장치의 양극에 긴 탄소봉(10~20 cm)을 부착하고 탄소봉의 끝에서 수 cm 떨어진 곳에 봉에 수직하게 흑연판을 놓는다.  에탄올, 탄화수소 가스 등의 탄소원 물질을 열플라즈마 장치에 연속적으로 주입하면 탄소원자 빔이 생성된다. 생성된 탄소원자 빔은 부착한 탄소봉을 따라 흐르면서 속도가 감소하고 균일하여진다. 균일한 탄소원자 빔이 적당한 에너지로 흑연판에 충돌할 때 흑연판의 표면 구조에 의한 에픽텔셜 성장으로 그래핀이 합성되는 방법이다. 합성된 그래핀은 흑연판에 연속적으로 충돌하는 Ar 기체 등에 의하여 벗겨져 챔버 안에 쌓이게 된다. 주입하는 탄소원 물질의 주입속도, 부착된 탄소봉의 내경 등의 조절을 통해 제조되는 그래핀의

두께와 크기를 대략적으로 조절할 수 있었다. 그리고 그래핀을 대량으로 생산하기 위해서는 주입하는 탄소원 물질의 주입속도를 증가시켜야 하는데 이럴 경우 제조되는 그래핀의 두께가 두꺼워 지는 문제가 발생한다. 이를 해결하기 위해 고정된 흑연판이 아닌 모터를 이용하여 회전하는 흑연판을 기판으로 사용하고 벗겨내기용 플라즈마 토치를 추가로 설치하여 그래핀이 두꺼워 지는 것을 방지 하였다. 그리고 탄소원 물질로 에틸렌 가스를 사용할 경우 100나노미터 정도의 작은 그래핀 조각이 제조되는데 이 그래핀 조각의 경우 일반적인 유기용매에 분산이 매우 잘 되는 성질이 있기 때문에 그래핀 용액을 제조하는데 매우 유리하면 다양한 분야로의 응용도 기대된다. 그리고 그래핀의 경우 크기가 100 나노미터 이하가 될 경우 일반적인 반도체 양자점과 같이 양자구속효과를 나타내는데 이를 그래핀 양자점이라고 정의한다. 그래핀 양자점의 경우 에너지 밴드갭이 0인 그래핀과 달리 에너지 밴드갭을 가지고 있기 때문에 좀 더 다양한 분야로 응용이 가능한 물질이다. 본 연구에서는 열플라즈마 장치를 이용하여 그래핀 양자점을 제조하는 방법도 개발하였는데 앞서 그래핀을 제조하는 방법의 경우 흑연판의 충돌에 의해 그래핀을 제조하였는데 이와는 다르게 과량의 탄소원 물질을 주입하여 탄소봉 내에서 탄소원자들간의 충돌로 그래핀 양자점을 제조 할 수 있었다. 제조된 그래핀 양자점의 경우 기존의 그래핀 양자점을 제조하는 방법과 비교하여 매우 간단한 방법으로 제조가 가능하며 짧은 시간내에 많은 양의 그래핀 양자점을 생산할 수 있는 장점이

있다. 또한 제조한 그래핀 양자점의 경우 광발광의 세기가 강하며 산소를 거의 포함하고 있지 않기 때문에 물성이 매우 뛰어나다고 여겨진다.